CHALMERS

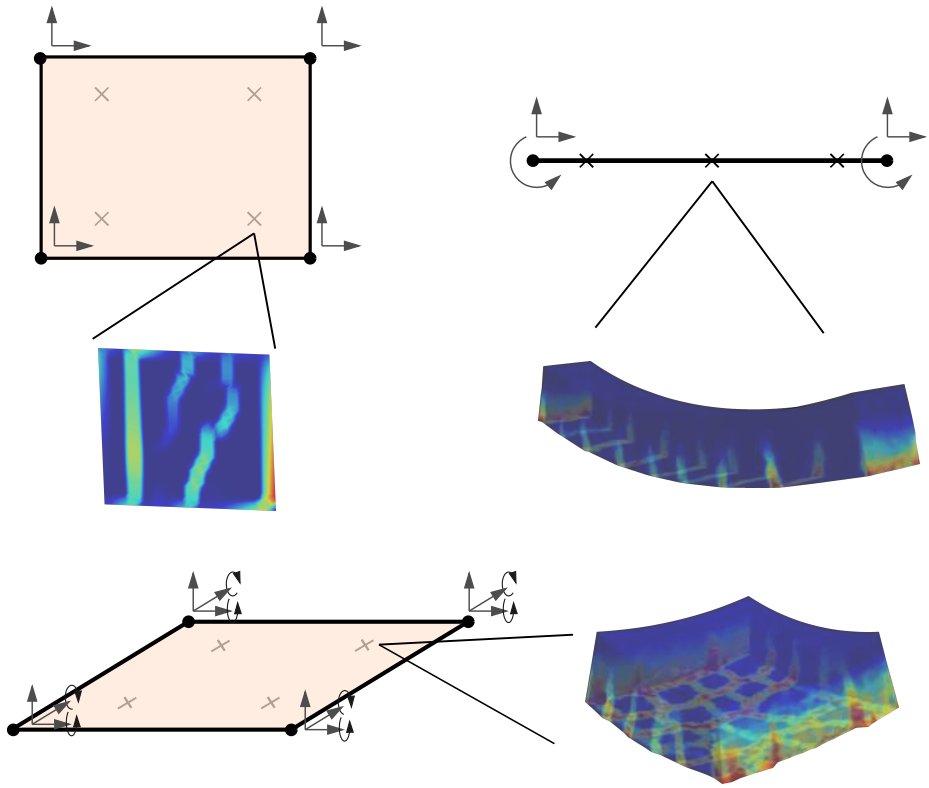

Multiscale Modelling of Reinforced Concrete Structures

ADAM SCIEGAJ

Department of Architecture and Civil Engineering
Department of Industrial and Materials Science
CHALMERS UNIVERSITY OF TECHNOLOGY
Gothenburg, Sweden 2020

THESIS FOR THE DEGREE OF DOCTOR OF PHILOSOPHY IN
SOLID AND STRUCTURAL MECHANICS

Multiscale Modelling of Reinforced Concrete Structures

ADAM SCIEGAJ

Department of Architecture and Civil Engineering
Department of Industrial and Materials Science
CHALMERS UNIVERSITY OF TECHNOLOGY

Gothenburg, Sweden 2020

Multiscale Modelling of Reinforced Concrete Structures
ADAM SCIEGAJ
ISBN 978-91-7905-238-6

Doktorsavhandlingar vid Chalmers tekniska högskola
Ny serie nr. 4705
ISSN 0346-718X
Department of Architecture and Civil Engineering
Department of Industrial and Materials Science
Chalmers University of Technology
SE-412 96 Gothenburg
Sweden
Telephone: +46 (0)31-772 1000

Cover:
Large-scale finite elements with corresponding Representative Volume Elements (RVEs) located at the large-scale integration points. Contour plots inside the RVEs represent the magnitude of the concrete strain tensor.

Chalmers Reproservice
Gothenburg, Sweden 2020

Multiscale Modelling of Reinforced Concrete Structures
Thesis for the degree of Doctor of Philosophy
ADAM SCIEGAJ
Department of Architecture and Civil Engineering
Department of Industrial and Materials Science
Chalmers University of Technology

Abstract

Concrete cracks at relatively low tensile stresses; cracks open up for ingress of harmful substances, negatively affecting the durability of reinforced concrete structures. Crack widths are thus limited in the design codes, and accurate predictions are needed, especially for large reinforced concrete structures such as bridges or nuclear reactor containment buildings. On the one hand, cracking of concrete, constitutive behaviour of steel, and the bond between them must be accounted for in order to properly describe crack growth. On the other hand, explicitly resolving these features in large structures could prove computationally intractable.

This thesis concerns multiscale modelling of reinforced concrete structures. More specifically, different two-scale models, based on Variationally Consistent Homogenisation (VCH), are developed. In these models, the response of a Representative Volume Element (RVE) is upscaled to a few popular structural models: a homogenised solid in plane stress, the effective Euler-Bernoulli beam and the effective Kirchhoff-Love plate. The effective response of the RVE is defined through a boundary value problem, for which different types of boundary conditions are developed and discussed. Furthermore, in order to allow for reinforcement slip transfer across the large-scale elements, a novel macroscopic reinforcement slip field is introduced.

The developed two-scale models are used to analyse reinforced concrete deep beams subjected to membrane loads, reinforced concrete beams subjected to uniaxial tension and bending, and reinforced concrete panels subjected to combinations of membrane and bending loads. The results show that the general structural behaviour is reflected well by the multiscale models compared to single-scale analyses.

By enriching the model with a macroscopic reinforcement slip field prescribed at the boundary of the RVE, the crack width predictions given by the two-scale models are improved and localisation of effective strain is observed at the large-scale. However, the results were dependent on the large-scale mesh and RVE sizes. In order to improve the objectivity of the model, a novel boundary condition type, prescribing the effective slip in the volume of the RVE, was developed. The macroscopic reinforcement slip became no longer RVE-size dependent, and the maximum crack width predictions were more consistent and showed a smaller variance for different large-scale meshes and sizes of RVEs.

In conclusion, the developed two-scale models allow for the analysis of a wide range of reinforced concrete structures, and show potential in saving computational time in comparison to single-scale analyses.

Keywords: multiscale, reinforced concrete, computational homogenisation, cracking, bond-slip

mojej rodzinie

Preface

The work in this thesis was carried out from August 2015 to January 2020, mostly at the Division of Structural Engineering, Department of Architecture and Civil Engineering and at the Division of Material and Computational Mechanics, Department of Industrial and Materials Science, both at Chalmers University of Technology. Part of this work was carried out during a research visit at University of Glasgow, from March to June 2019. The research was financially supported by the Swedish Research Council (Vetenskapsrådet) under grants 2014-5168 and 2018-03691. Some of the numerical simulations presented herein were performed on resources at the Chalmers Centre for Computational Science and Engineering (C3SE) provided by the Swedish National Infrastructure for Computing (SNIC).

Acknowledgements

I am most grateful to my excellent supervisors Professor Karin Lundgren, Professor Fredrik Larsson, and Professor Kenneth Runesson. Had it not been for your constant willingness to help and readiness to share your insight and experience, this thesis would not have seen the light of day. Your encouragement and feedback made it possible for me to progress within this research area, and for that I will always be thankful.

Moving on, I would like to acknowledge Dr. Filip Nilenius for his help, especially in the initial phase of the project. Having a similar research background, you knew what I was getting myself into, and were always ready to help. In addition, I want to thank Dr. Peter Grassl for hosting me in Glasgow and dedicating some of his time to this research project. Your expertise in using OOFEM for modelling reinforced concrete has been very valuable to me.

Furthermore, I would like to express my gratitude to my dear friends and colleagues (you're too many to list here – you know who you are!) both at and outside Chalmers. You created a very stimulating and friendly environment. Thank you for all the interesting discussions and activities I could be part of, both during and after work. I will never forget that.

Finally, I would like to thank my parents and my brother for their love and unwavering support, especially when I was stuck on some persisting problem. I could always count on your support, predominantly in times of doubt. Dziękuję!

Gothenburg, January 2020

Adam Ścięgaj

Thesis

This thesis consists of an extended summary and the following appended papers:

Paper A A. Sciegaj, F. Larsson, K. Lundgren, F. Nilenius and K. Runesson (2018). "Two-scale finite element modelling of reinforced concrete structures: Effective response and subscale fracture development" *International Journal for Numerical Methods in Engineering, 114(10)*, 1074–1102. DOI: 10.1002/nme.5776

Paper B A. Sciegaj, F. Larsson, K. Lundgren, F. Nilenius and K. Runesson (2019). "A multiscale model for reinforced concrete with macroscopic variation of reinforcement slip" *Computational Mechanics, 63(2)*, 139–158. DOI: 10.1007/s00466-018-1588-3

Paper C A. Sciegaj, F. Larsson, K. Lundgren and K. Runesson (2019). "On a volume averaged measure of macroscopic reinforcement slip in two-scale modeling of reinforced concrete" *International Journal for Numerical Methods in Engineering*, in press. DOI: 10.1002/nme.6288

Paper D A. Sciegaj and A. Mathern (2019). "Two-scale modelling of reinforced concrete deep beams: Choice of unit cell and comparison with single-scale modelling" In *A. Zingoni (Ed.), Advances in Engineering Materials, Structures and Systems: Innovations, Mechanics and Applications*, 251–256, CRC Press, DOI: 10.1201/9780429426506

Paper E A. Sciegaj, P. Grassl, F. Larsson, K. Runesson and K. Lundgren. "Upscaling of three-dimensional reinforced concrete representative volume elements to effective beam and plate models" *Submitted for publication*

The appended papers were prepared in collaboration with the co-authors.

For Papers A, B, and C, the author of this thesis was responsible for the major progress of the work in the papers, i.e., took part in formulating the theory, led the planning of the papers, developed the numerical implementation, carried out the numerical simulations, and prepared the manuscript.

For Paper D, the two co-authors jointly initiated and planned the study. The author of this thesis was the principal author of the paper and was responsible for carrying out the two-scale simulations and writing the manuscript. The second author carried out the single-scale simulations and contributed to writing of the paper.

For Paper E, the author of this thesis was responsible for the major progress of the work in the paper, i.e., took part in formulating the theory and developing the numerical implementations, led the planning of the paper, carried out the bulk of the numerical simulations and prepared the manuscript.

Other publications by the author

Conference proceedings

- A. Sciegaj, F. Larsson, K. Lundgren, F. Nilenius, and K. Runesson. "Two-scale modelling of reinforced concrete". *29th Nordic Seminar on Computational Mechanics*. Ed. by R. Larsson. Gothenburg, 2016.
- A. Sciegaj, P. Grassl, F. Larsson, K. Lundgren, and K. Runesson. "On periodic boundary conditions in Variationally Consistent Homogenisation of beams and plates". *32nd Nordic Seminar on Computational Mechanics*. Ed. by A. H. Niemi. Oulu, 2019.
- A. Sciegaj, F. Larsson, K. Lundgren, and K. Runesson. "On the micro-to-macro transition of reinforcement slip in two-scale modelling". *10th International Conference on Fracture Mechanics of Concrete and Concrete Structures*. Ed. by Pijaudier-Cabot, G. and Grassl, P. and La Borderie, C. Bayonne, 2019. DOI: 10.21012/FC10.235337.

Licentiate thesis

- A. Sciegaj. *Multiscale Modelling of Reinforced Concrete*. Licentiate Thesis. Chalmers University of Technology, 2018.

Popular science papers

- A. Sciegaj, K. Lundgren, F. Larsson, F. Nilenius, and K. Runesson. Ny metod för sprickmodellering i armerad betong. *Bygg & Teknik* **110**.7 (2018), 46–48.

Contents

Part I
Extended Summary

1 Introduction

1.1 Background

Reinforced concrete is the most widely used construction material in the world, and the use of it is forecast to increase in the future [16]. Even though concrete cracks at relatively low tensile stresses, the structure does not fail as the steel reinforcement can carry the stresses. However, the durability of the structure can be negatively affected by this, as cracks open up the cross-section for ingress of harmful substances causing corrosion of the steel [74]. As a result, the crack widths are limited in design codes [11], and accurate prediction methods are needed. Even though good analytical and numerical models exist [101, 34, 20, 42], the task is challenging especially for large-scale structures with complex shape and loading such as bridges and nuclear reactor containments [9, 43, 83, 32, 33].

In order to properly describe the cracking process in concrete, a model accounting for strain localisation in plain concrete, constitutive response of reinforcement, and bond-slip behaviour in the interface is needed. However, explicitly modelling these fine-scale features in the whole structure can prove computationally infeasible due to the size of the model. In recent years, multiscale modelling methods have been gaining popularity. In particular, methods based on computational homogenisation [64] allow for obtaining accurate fine-scale results at a fraction of the computational cost of the single-scale models. In these methods, the microstructure of the material is statistically represented by an appropriately sized volume, also referred to as the Representative Volume Element (RVE). Even though advanced multiscale models have been developed for plain concrete [69, 72, 75, 107, 47], their application to reinforced concrete has not been considered to the same extent.

1.2 Aim of research

The aim of this research was to extend the multiscale modelling methodology to reinforced concrete. The goal was to enable the study of crack development for large-scale structures, and thus, the serviceability limit state was to be considered. To this end, the following questions were of interest:

- Is it possible to use computational homogenisation to model cracking in reinforced concrete structures?
- What kind of boundary conditions are most suitable for the RVE problem?
- Is it possible to upscale the response of the RVe to commonly used structural models?

- What is the significance of reinforcement slip in two-scale modelling?
- How can the slip be treated in computational homogenisation and how do the different options affect the results?
- How well, compared to single-scale models, do two-scale models predict the global structural behaviour and local crack development?

1.3 Method

In order to answer the previously stated research questions, the following tasks were identified and carried out in this work:

- To establish a variationally consistent framework for two-scale analysis of reinforced concrete.
- To create a numerical model of the reinforced concrete RVE.
- To upscale the response of reinforced concrete RVEs to effective solid, beam and plate models.
- To investigate the effect of different boundary conditions for the reinforced concrete RVE problem.
- To implement an FE^2 (Finite Element squared) algorithm for numerical two-scale analyses of reinforced concrete structures.
- To incorporate the macroscopic reinforcement slip variable into the two-scale model and study the effect of it.
- To evaluate the performance of the two-scale analyses with respect to conventional single-scale analyses.

1.4 Scope and limitations

The main focus of this work was to develop multiscale modelling techniques for reinforced concrete. Throughout this work, it is assumed that plain concrete can be represented as a homogeneous material, i.e., the mesoscopic features of concrete are omitted. The reinforcement is assumed to be adequately represented with either beam (**Papers A, B, C, E**) or truss (**Paper D**) elements. Furthermore, only first order computational homogenisation is considered, i.e., the macroscopic parts of the total fields vary linearly within the RVEs. With regard to structures, this work treated mainly concrete structures with uniformly distributed reinforcement layout, but a few examples of non-uniformly reinforced structures were also considered in **Paper D**. Regarding load duration, no dynamic response was simulated, as only quasi-static loading was considered. Since crack widths are of interest, serviceability limit state was the main focus of the work. As such, accurate modelling of structural failure due to macroscopic localisation was considered to be out of the scope of this thesis.

1.5 Numerical implementation

Verification of the performance of the developed methodology was carried out through the aid of numerical examples. To this end, the numerical algorithms were implemented by the author of this thesis in the following software:

- The two-scale models were implemented in OOFEM [79], an object-oriented open source C++ finite element solver. The Git repository containing the source code along with numerous test examples is available at `https://github.com/adsci/oofem`.
- Pre-processing of both macroscopic models and subscale unit cells was performed in SALOME, an open-source pre- and post-processing platform for numerical simulation, available at `https://www.salome-platform.org/`. The platform-provided Python interface allows for automatic mesh generation. The unv2oofem converter, included in the OOFEM distribution, was used for mesh conversion to OOFEM-native format.
- The post-processing was done with Paraview (`https://www.paraview.org/`), GNU Octave (`https://www.gnu.org/software/octave/`) and pgfplots, a LaTeX package for creating scientific graphs.

2 Cracking in reinforced concrete

The problem of cracking in concrete spans multiple length scales, as it ranges from diffused microcracks to localised failure [106], making accurate modelling thereof challenging. In contrast to plain concrete, reinforced concrete does not fail structurally, as tensile stresses are carried by the steel reinforcement after cracking of concrete. As a result, several cracks can form before the structure fails due to ultimate load. At moderate load levels (serviceability limit state) cracks are common and expected. A very important mechanism governing the fracture development is the stress transfer in the steel/concrete interface. Therefore, the bond between concrete and reinforcement must also be considered in modelling [25].

2.1 Localised failure in plain concrete

Localised failure in tension can be illustrated with a uniaxial tensile test, cf. Figure 2.1. At first, microscopic cracks start to nucleate at inhomogeneities in the aggregate-cement interphase due to tensile stresses. As the load increases, the incipient microcracks coalesce into a distinct fracture zone at the weakest section of the specimen. When the stresses reach the tensile strength, we enter the softening regime and the deformations further increase while the material outside of the fracture zone experiences unloading. The diffuse fracture zone eventually evolves into a macroscopic crack and the material breaks, allowing no further stress transfer between the parts.

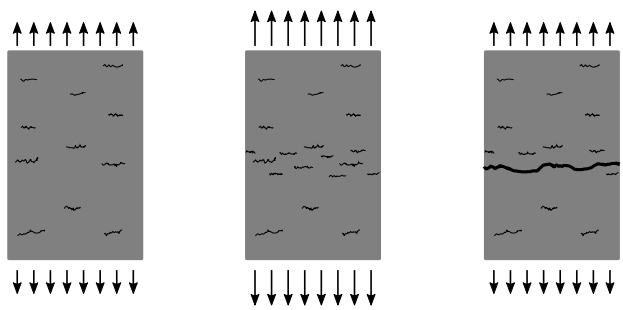

Figure 2.1: Fracture development in a concrete specimen subjected to tensile load.

In modelling of fracture, there exist numerous ways to represent the fracture zone, depending on the regularity of the displacement and strain fields, denoted $\boldsymbol{u}(\boldsymbol{x})$ and $\boldsymbol{\varepsilon}(\boldsymbol{x})$, respectively. Usually, three main types of strain discontinuity are considered: *strong discontinuity*, *weak discontinuity* and *continuous* strain field (no discontinuity), see [44] for an extensive review and Table 2.1 for an overview.

Strong discontinuity is represented by a displacement jump, and the strain field comprises regular and singular parts. Cohesive zone models or discrete crack models [37, 103, 78, 92, 93], defining the traction-separation law of the crack are usually used to model this type of localisation. In the finite element setting, interface elements can be used to

Table 2.1: *Overview of models for strain localisation.*

Strain regularity	Strong discontinuity	Weak discontinuity	Continuity
Kinematic representation	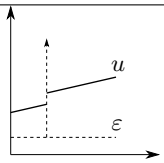	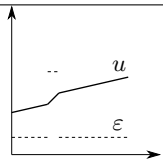	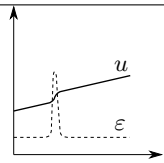
Constitutive models	cohesive zone models/discrete crack models	smeared crack models	nonlocal/gradient enriched continua
Finite element implementation	interface elements, embedded discontinuity elements (ED-FEM), extended finite element method (XFEM)	standard elements, special elements with embedded localisation bands	standard elements, special enriched elements

model a strong discontinuity in a straight-forward way, but the location and propagation path of the crack need to be known in advance. Alternatively, elements with embedded discontinuity (ED-FEM) [65, 41, 71, 54, 8] or the extended finite elements (XFEM) [5, 28], based on enrichment of the standard shape functions, can be used.

A weak discontinuity formulation considers a localisation band with a finite width. While the displacement field remains continuous, a jump in strain field can be observed. In contrast to the previous approach, no distinct separation can be seen in the model, and the crack is represented by a band of high strains. The size of this band is often denoted the *crack band width* [4, 3]. The previously discussed traction-separation law is replaced by a stress-strain relation within the band, constituting a smeared crack model [88, 89, 19]. Smeared crack models are very popular in modelling of concrete structures, as they are compatible with standard finite elements and are relatively straight-forward to implement. Even though many constitutive models for tensile fracture can be used in smeared crack setting [46, 77, 18, 30, 91], regularisation of the models with respect to mesh size is necessary in order to provide mesh-independent result. More specifically, the model must be calibrated to the chosen band width, h, so that the fracture energy of concrete, G_{F}, is preserved. In this work, isotropic damage models [62, 61] were used to simulate the response of concrete under load, see Figure 2.2 for an example of stess–strain response.

The third formulation ensures continuity of displacement and strain fields. The strains are then localised in a narrow band of larger strains, and there is no strain discontinuity between the band and the surrounding material. Strain fields fulfilling these criteria can be reproduced by advanced constitutive models based on nonlocal or gradient enriched continua [45, 80, 31]. However, the discretisation of the domain must be rather fine in order to resolve large strain gradients. Alternatively, special enrichments of the elements

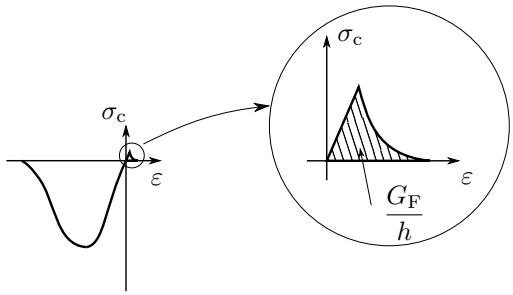

Figure 2.2: Uniaxial stress–strain (σ_c–ε) relation for concrete given by the Mazars continuum damage model [62]. Here, G_F corresponds to the fracture energy, and h to the chosen crack band width.

can be employed to allow for a coarser mesh.

It is noteworthy, that even though the discussion in this section pertained mainly to strain localisation in tension, a similar physical phenomenon is observed for concrete in compression, where concrete is crushed under excessive compressive strains. Since the focus of this work is put on serviceability limit states, compressive failure of concrete is not included in the used constitutive models.

2.2 Elastoplasticity of reinforcement

In this work, the reinforcement is considered to be subjected to both normal forces and bending moments. It is therefore modelled with classical beam elements, with the exception of **Paper D**, where it is simplified to truss elements. Plasticity is introduced by an elastoplastic constitutive model based on Von Mises yield criterion. The model used in this work considers linear isotropic strain hardening driven by the cumulative plastic strain, see Figure 2.3 for a typical uniaxial stress–strain curve. Similarly to concrete, the failure of the material (steel rupture at ultimate strain) is not considered in this work due to the focus on serviceability limit state.

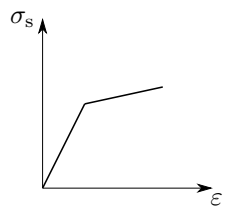

Figure 2.3: Stress–strain (σ_s–ε) relation for steel using an elastoplastic model with hardening.

2.3 Bond between concrete and reinforcement

The bond between concrete and reinforcement results from three mechanisms: chemical adhesion, friction, and mechanical interlocking [1, 7]. As the contribution from chemical adhesion is small, it is lost as soon as the slip (difference in displacements) between steel and concrete builds up [25]. Subsequently, stresses between reinforcement ribs and the

neighbouring concrete develop. The traction on the inclined interface can be decomposed into longitudinal and radial components, denoted *bond* and *splitting* stresses, respectively. It is noteworthy, that the presence of the splitting stresses is necessary for bond stress transfer after the loss of chemical adhesion.

In reinforced concrete structures modelling, the steel/concrete bond is often taken into account by a suitable bond-slip model relating the bond stresses to reinforcement slip [17, 67]. Such models, although simplifying the complex mechanical behaviour of the interface, provide a good approximation. Generally, two types of failure can occur in the steel/concrete interface: splitting and pull-out failure. Splitting failure occurs when the concrete surrounding the steel bar cracks, and not enough transverse reinforcement is present. Conversely, if the concrete around the rebar is well-confined, i.e., when a large concrete cover and dense transverse reinforcement or transverse compression are present, a pull-out failure can be observed. The splitting and pull-out failure constitute the lower and upper bounds, respectively, of the bond capacity. The bond-slip model used in this work [26] assumes a pull-out failure, see Figure 2.4.

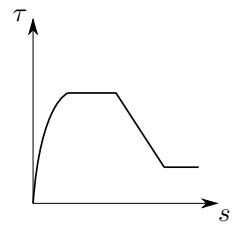

Figure 2.4: Example of bond-slip (τ–s) relation at reinforcement pull-out.

For the numerical implementation, a few different finite element models have been used to model the bond. A popular choice is to use interface elements and resolve the steel/concrete interface. As the bond-slip law includes the effect of the ribs, there is no need to explicitly resolve the inclined surfaces of the interface. The bond-slip relation is then used as the constitutive traction-separation input in the tangential direction [56, 55, 57]. Alternatively, suitable enrichments of the finite elements used to model the structure can be considered to allow for capturing the strain difference between concrete and reinforcement [41, 21, 22, 40, 15, 27].

2.4 Response of a cracked reinforced concrete tie

As already alluded to, cracking of concrete does not result in structural failure of a reinforced concrete member. Consequently, the load is still carried by the member even after the concrete has cracked, see Figure 2.5, where the response of a cracked reinforced concrete tie is shown.

Far away from the cracks (starting from the left side of the figure), the reinforcement can be assumed to be perfectly bonded with concrete. Consequently, no slip is present there, and both concrete and steel carry a portion of the load, corresponding to their stiffness ratio. Moving closer towards the crack, the slip starts building up as the difference in deformations becomes more apparent. In the vicinity of the crack the concrete unloads until it is stress-free at the crack face, and the reinforcement takes up more load so that equilibrium is fulfilled. At the crack face, the whole force is carried by the reinforcement, and a relatively large value of the slip can be observed. On the other side of the crack we have an analogous situation with the slip having an opposite sign. As we move further away from the crack face (to the right), the stresses are transferred from the reinforcement

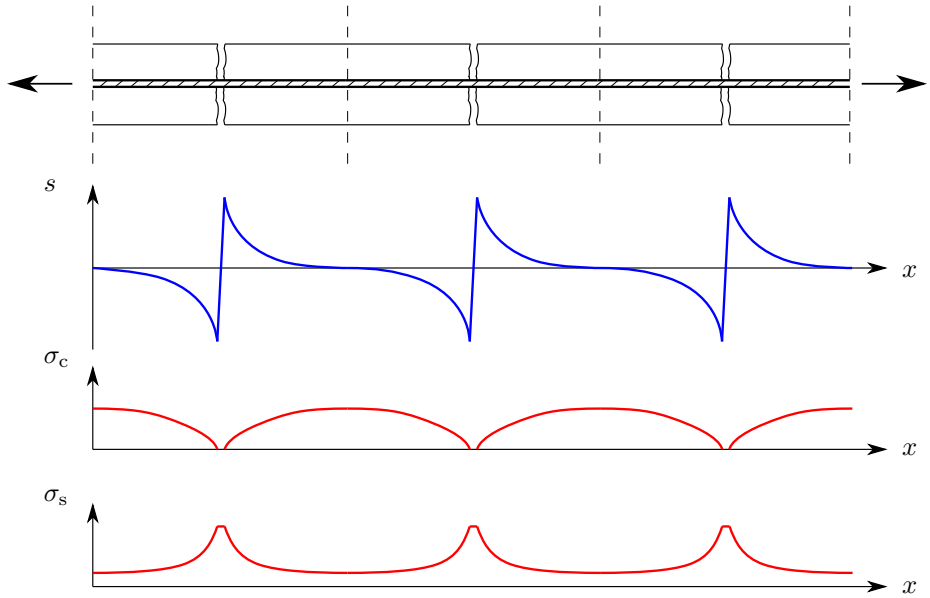

Figure 2.5: Variation of slip, s, concrete and steel stress, σ_c and σ_s, respectively, in a cracked reinforced concrete tie.

bars to the the uncracked concrete via bond stresses in the interface. Note that the sum of the forces carried by steel and concrete is constant along the member. Furthermore, the slip distribution can be used to easily identify the locations of the cracks, which are indicated by large gradients of the slip with the slip changing sign.

3 Fine-scale model for reinforced concrete

Prior to introducing the multiscale modelling techniques, the fully-resolved model of reinforced concrete used in this work, is briefly outlined. The problem domain, Ω, is split into the concrete and reinforcement part, i.e., $\Omega = \Omega_\mathrm{c} \cup \Gamma_\mathrm{int}$, while the problem boundary, Γ_ext, is decomposed into the essential and natural boundaries, i.e., $\partial\Omega = \Gamma_\mathrm{ext} = \Gamma_\mathrm{u} \cup \Gamma_\mathrm{t}$. The concrete is assumed to be a continuum subjected to body forces $\hat{\boldsymbol{b}}$ in Ω_c and tractions $\hat{\boldsymbol{t}}$ on Γ_t. The spatial arrangement of each reinforcement bar can be defined with unit vector $\boldsymbol{e}_\mathrm{l}$ in the longitudinal direction, and unit vectors $\boldsymbol{e}_{\perp,\mathrm{i}}$ in the transverse directions, cf. Figure 3.1.

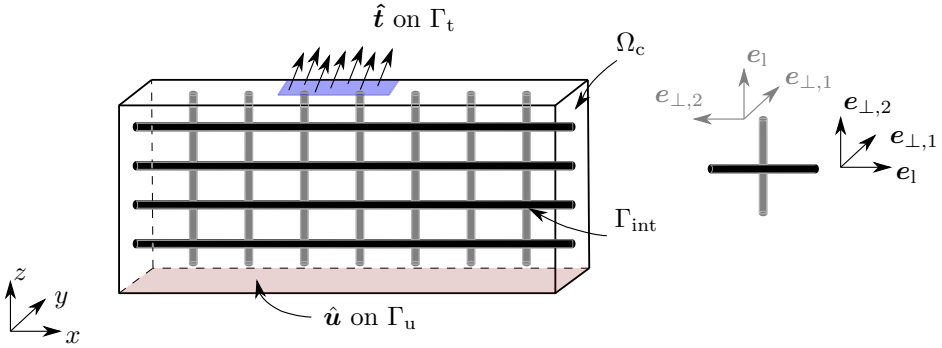

Figure 3.1: A general reinforced concrete structure. For each reinforcement bar, longitudinal and transverse unit vectors $\boldsymbol{e}_\mathrm{l}$ and $\boldsymbol{e}_{\perp,\mathrm{i}}$ are defined.

The unknown displacement fields in steel ($\boldsymbol{u}_\mathrm{s}$) and concrete ($\boldsymbol{u}_\mathrm{c}$) can be decomposed into the longitudinal and transverse components as

$$\begin{aligned} \boldsymbol{u}_{\mathrm{s,l}} &= u_{\mathrm{s,l}}\boldsymbol{e}_\mathrm{l}, \qquad \boldsymbol{u}_{\mathrm{c,l}} = u_{\mathrm{c,l}}\boldsymbol{e}_\mathrm{l}, \\ \boldsymbol{u}_{\mathrm{s},\perp} &= \boldsymbol{I}_\perp \cdot \boldsymbol{u}_\mathrm{s}, \quad \boldsymbol{u}_{\mathrm{c},\perp} = \boldsymbol{I}_\perp \cdot \boldsymbol{u}_\mathrm{c}, \end{aligned} \tag{3.1}$$

where the tensor $\boldsymbol{I}_\perp = [\boldsymbol{I} - \boldsymbol{e}_\mathrm{l} \otimes \boldsymbol{e}_\mathrm{l}]$ extracts the transversal part of displacement vector. Reinforcement slip, $s = u_{\mathrm{s,l}} - u_{\mathrm{c,l}}$, gives rise to bond stresses along the bar, t_Γ, which are distributed around the perimeter S_s. The bars are also subjected to transverse loads $\boldsymbol{\lambda}$ acting in the transverse directions. Additionally, it is assumed that there is no reinforcement slip in the transverse direction, i.e. $\boldsymbol{u}_{\mathrm{s},\perp} = \boldsymbol{u}_{\mathrm{c},\perp}$ all along the bars.

Considering small strain setting and quasi-static loading, the strong form of the equilibrium equations is given by

$$\begin{aligned} -\boldsymbol{\sigma}_{\mathrm{c}} \cdot \boldsymbol{\nabla} &= \hat{\boldsymbol{b}} \quad \text{in } \Omega_{\mathrm{c}}, \\ -\frac{\partial N_{\mathrm{s}}}{\partial l} + S_{\mathrm{s}} t_{\Gamma} &= 0 \quad \text{in } \Gamma_{\mathrm{int}}, \\ -\frac{\partial^2 \boldsymbol{M}_{\mathrm{s}}}{\partial l^2} + \boldsymbol{\lambda} &= 0 \quad \text{in } \Gamma_{\mathrm{int}}, \\ \boldsymbol{u}_{\mathrm{s},\perp} - \boldsymbol{u}_{\mathrm{c},\perp} &= \boldsymbol{0} \quad \text{in } \Gamma_{\mathrm{int}}, \\ \boldsymbol{u} &= \hat{\boldsymbol{u}} \text{ on } \Gamma_{\mathrm{u}}, \\ \boldsymbol{\sigma}_{\mathrm{c}} \cdot \boldsymbol{n} &= \hat{\boldsymbol{t}} \quad \text{on } \Gamma_{\mathrm{t}}, \\ N_{\mathrm{s}} = 0,\ \boldsymbol{T}_{\mathrm{s}} = \boldsymbol{M}_{\mathrm{s}} &= \boldsymbol{0} \text{ on } \partial\Gamma_{\mathrm{int}}, \end{aligned} \tag{3.2}$$

where $\boldsymbol{\sigma}_{\mathrm{c}}$ is the Cauchy stress in concrete, $\boldsymbol{\nabla}$ is the gradient operator, $\boldsymbol{n}$ is a unit normal vector, N_{s} is the normal force in the rebar and $\boldsymbol{T}_{\mathrm{s}}$ and $\boldsymbol{M}_{\mathrm{s}}$ are the shear forces and bending moments in the rebars, respectively.

The equilibrium in the steel–concrete interface, schematically depicted in Figure 3.2, can be expressed as

$$[[\boldsymbol{\sigma}_{\mathrm{c}}]] \cdot \boldsymbol{e}_{\perp,1} H_2 + [[\boldsymbol{\sigma}_{\mathrm{c}}]] \cdot \boldsymbol{e}_{\perp,2} H_1 + \boldsymbol{\lambda} + S_{\mathrm{s}} t_{\Gamma} \boldsymbol{e}_{\mathrm{l}} = \boldsymbol{0}, \tag{3.3}$$

where $[[\boldsymbol{\sigma}_{\mathrm{c}}]] := \boldsymbol{\sigma}_{\mathrm{c}}^{+} - \boldsymbol{\sigma}_{\mathrm{c}}^{-}$ denotes the jump in the stresses across the interface and $H_1 \times H_2$ define a cut-out region surrounding the reinforcement bar.

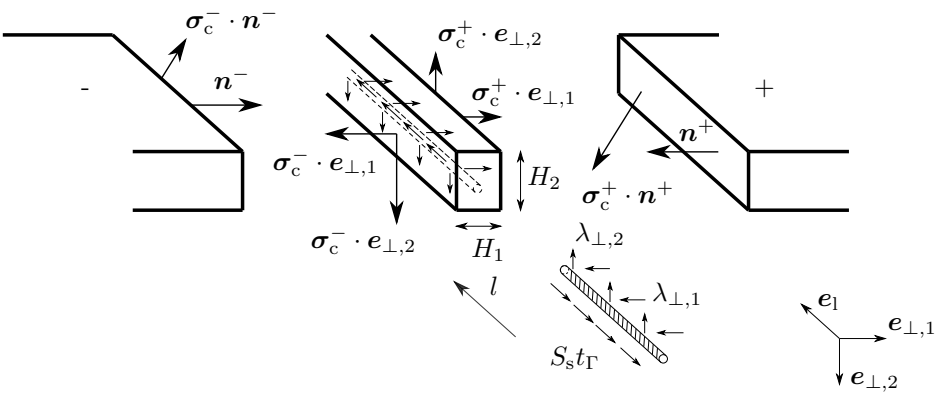

Figure 3.2: Steel–concrete interface. Boundary forces on the rebar cut out and concrete boundary tractions omitted.

With the help of (3.3), the weak form of the equilibrium equations (3.2) is obtained as: Find $\boldsymbol{u}_\mathrm{c}, u_\mathrm{s,l}, \boldsymbol{u}_\mathrm{s,\perp}, \boldsymbol{\lambda} \in \mathbb{U}_\mathrm{c} \times \mathbb{U}_\mathrm{s,l} \times \mathbb{U}_\mathrm{s,\perp} \times \mathbb{L}$ such that

$$
\begin{aligned}
\int_{\Omega_\mathrm{c}} \boldsymbol{\sigma}_\mathrm{c} : [\delta \boldsymbol{u}_\mathrm{c} \otimes \boldsymbol{\nabla}] \ \mathrm{d}\Omega - \int_{\Gamma_\mathrm{int}} [S_\mathrm{s} t_\Gamma \boldsymbol{e}_\mathrm{l} + \boldsymbol{\lambda} \cdot \boldsymbol{I}_\perp] \cdot \delta \boldsymbol{u}_\mathrm{c} \ \mathrm{d}\Gamma = \\
\int_{\Gamma_\mathrm{ext}} \hat{\boldsymbol{t}} \cdot \delta \boldsymbol{u}_\mathrm{c} \ \mathrm{d}\Gamma + \int_{\Omega_\mathrm{c}} \hat{\boldsymbol{b}} \cdot \delta \boldsymbol{u}_\mathrm{c} \ \mathrm{d}\Omega \qquad \forall \ \delta \boldsymbol{u}_\mathrm{c} \in \mathbb{U}_\mathrm{c}^0, \\
\int_{\Gamma_\mathrm{int}} N_\mathrm{s} \frac{\partial \delta u_\mathrm{s,l}}{\partial l} + S_\mathrm{s} t_\Gamma \delta u_\mathrm{s,l} \ \mathrm{d}\Gamma = 0 \qquad \forall \ \delta u_\mathrm{s,l} \in \mathbb{U}_\mathrm{s,l}, \\
- \int_{\Gamma_\mathrm{int}} \boldsymbol{M}_\mathrm{s} \cdot \frac{\partial^2 \delta \boldsymbol{u}_\mathrm{s,\perp}}{\partial l^2} + \boldsymbol{\lambda} \cdot \delta \boldsymbol{u}_\mathrm{s,\perp} \ \mathrm{d}\Gamma = 0 \qquad \forall \ \delta \boldsymbol{u}_\mathrm{s,\perp} \in \mathbb{U}_\mathrm{s,\perp}, \\
\int_{\Gamma_\mathrm{int}} [\boldsymbol{u}_\mathrm{s,\perp} - \boldsymbol{I}_\perp \cdot \boldsymbol{u}_\mathrm{c}] \cdot \delta \boldsymbol{\lambda} \ \mathrm{d}\Gamma \ = 0 \qquad \forall \ \delta \boldsymbol{\lambda} \in \mathbb{L},
\end{aligned}
\tag{3.4}
$$

for suitably defined trial and test spaces. The result in (3.4) is independent of $H_1 \times H_2$ if it is assumed that Ω_c does not exclude the cut-out region. In the continuous setting, the displacement field in the concrete formally has to be regularised when comparing to the beam elements in order to avoid artificial singularities. However, in this work, we restrict to coarse meshes, whereby we assume that the finite elements of the concrete are larger than the physical dimensions of the reinforcement cross-section. The fully-resolved three-dimensional formulation presented above was used in **Paper E**. In **Papers A**–**D**, the formulation was simplified to two dimensions. Thus, only one unit vector $\boldsymbol{e}_\perp$ is considered for each rebar. Additionally, M_s, T_s, λ, $u_\mathrm{s,\perp}$ and $u_\mathrm{c,\perp}$ can all be represented with scalar values.

4 Computational Multiscale Modelling

4.1 Overview of multiscale methods

When modelling large-scale structures, it is necessary to have a suitable macroscopic constitutive model of the material. Due to practical reasons, it is often desired to simplify the representation of the material, e.g. by assuming it to be is macroscopically homogeneous. However, the actual physical phenomena within the material usually take place at smaller length scales. If the physical phenomena on smaller scales are completely omitted, the results provided by the model might prove excessively inaccurate. On the other hand, modelling the whole structure at the detailed fine-scale level might prove infeasible in practice. Hence, it is important to incorporate the subscale physics into the large-scale models without explicitly resolving every fine-scale detail. Depending on how the information is passed between the scales, multiscale methods can be divided into *hierarchical* an *concurrent* methods [6, 60]. Depending on the direction of information transfer between the scales, hierarchical methods are further subdivided into *coupled* and *uncoupled* hierarchical methods [105], see Figure 4.1.

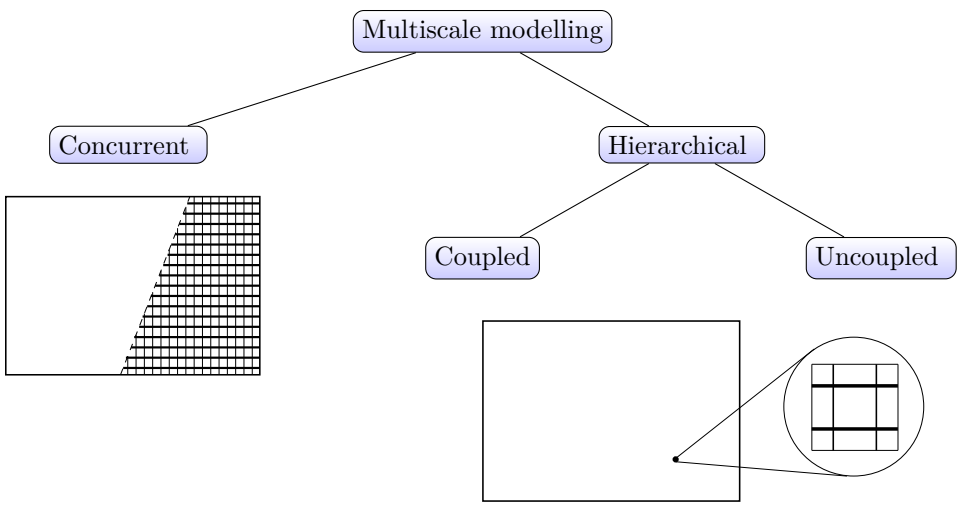

Figure 4.1: Classification of the multiscale modelling methods. The work in this thesis can be classified as coupled hierarchical multiscale modelling.

In concurrent methods, the fine-scale model is embedded in the coarse-scale model in a specific region of interest, enforcing equilibrium and compatibility along the micro-macro interface [58]. Both of the models are then solved simultaneously, allowing for unrestrained exchange of information in both directions between the scales. Concurrent multiscale modelling has been used to study localised failure [90] in plain concrete [105, 94, 87] and reinforced concrete frames and beams [96, 95, 59]. However, structures that

display distributed cracking, e.g. due to presence of uniform reinforcement in the form of reinforcement grids, would eventually require fine resolution in the whole problem domain, thus making the proposed method infeasible in practice due to computational effort.

In hierarchical methods, parts of the problem domain are occupied by multiple scales simultaneously. The scales are then linked with each other by means of averaging theorems (homogenisation) or parameter identification. Uncoupled hierarchical methods generally allow for transfer of information only in one direction, i.e., from the fine-scale to the large-scale model. For example, the fine-scale response can be computed *a priori* and stored for future use by the macroscopic model. Macroscopic parameter identification from subscale simulations and classical homogenisation are important examples of methods falling within this category. Uncoupled hierarchical multiscale methods have been used in application to plain and reinforced concrete in [50, 51, 39, 82, 53, 10, 68].

In coupled hierarchical methods (also called the semi-concurrent methods) the transfer of information goes in between the scales in both directions. Usually, the fine-scale model is asked for the response given a specific large-scale input. The subscale response is then homogenised to a fitting macroscopic format and sent to the large-scale model for further analysis. In contrast to uncoupled hierarchical methods, storage of the coarse-scale phenomenological data is not necessary, as the subscale model takes the role of a sophisticated constitutive driver. These methods have been widely applied to model sandwich structures [48, 86, 12], masonry [63, 81] and reinforced concrete hollow-core slabs [66] An example of an approach falling within this category is the FE^2 (Finite Element squared) method [24, 23], which is used to analyse reinforced concrete structures in multiscale manner in **Papers A–E**.

4.2 Variationally consistent homogenisation

In order to develop a suitable multiscale modelling scheme, we employ the concept of Variationally Consistent Homogenisation (VCH) [52] for the standard first-order homogenisation. To this end, a macroscopically homogeneous solid occupying the domain $\bar{\Omega}$ is considered. The solid has a heterogeneous microstructure. In the reinforced concrete setting used in this work, the subscale heterogeneity is represented by distinct reinforcement bars and the interface between them and the concrete. However, for the purpose of illustration of the VCH, a simpler problem pertaining only to concrete solid (corresponding to the first equation in 3.2), is considered here:

$$\int_{\Omega_\mathrm{c}} \boldsymbol{\sigma}_\mathrm{c} : [\delta \boldsymbol{u}_\mathrm{c} \otimes \boldsymbol{\nabla}] \ \mathrm{d}\Omega = \int_{\Gamma_\mathrm{ext}} \hat{\boldsymbol{t}} \cdot \delta \boldsymbol{u}_\mathrm{c} \ \mathrm{d}\Gamma + \int_{\Omega_\mathrm{c}} \hat{\boldsymbol{b}} \cdot \delta \boldsymbol{u}_\mathrm{c} \ \mathrm{d}\Omega \quad \forall \ \delta \boldsymbol{u}_\mathrm{c} \in \mathbb{U}_\mathrm{c}^0. \tag{4.1}$$

The goal of the multiscale method is to solve for the macroscopically smooth displacement field $\bar{\boldsymbol{u}}$ without explicit resolution of the microscopic details on the macroscale. As a first step, the so-called Variational MultiScale (VMS) split [38] is applied, where the total displacement field $\boldsymbol{u}$ is decomposed into macroscopic ($\boldsymbol{u}^M$) and subscale ($\boldsymbol{u}^s$) parts, i.e., $\boldsymbol{u} = \boldsymbol{u}^M + \boldsymbol{u}^s$. This way, the original problem in eq. (4.1) is replaced by the *macro*

problem

$$\int_{\Omega_c} \boldsymbol{\sigma}_c : \left[\delta \boldsymbol{u}_c^M \otimes \boldsymbol{\nabla}\right] \, \mathrm{d}\Omega = \int_{\Gamma_{ext}} \hat{\boldsymbol{t}} \cdot \delta \boldsymbol{u}_c^M \, \mathrm{d}\Gamma + \int_{\Omega_c} \hat{\boldsymbol{b}} \cdot \delta \boldsymbol{u}_c^M \, \mathrm{d}\Omega \quad \forall \, \delta \boldsymbol{u}_c^M \in \mathbb{U}_c^{M,0}, \tag{4.2}$$

and the *subscale problem*

$$\int_{\Omega_c} \boldsymbol{\sigma}_c : \left[\delta \boldsymbol{u}_c^s \otimes \boldsymbol{\nabla}\right] \, \mathrm{d}\Omega = \int_{\Gamma_{ext}} \hat{\boldsymbol{t}} \cdot \delta \boldsymbol{u}_c^s \, \mathrm{d}\Gamma + \int_{\Omega_c} \hat{\boldsymbol{b}} \cdot \delta \boldsymbol{u}_c^s \, \mathrm{d}\Omega \quad \forall \, \delta \boldsymbol{u}_c^M \in \mathbb{U}_c^s. \tag{4.3}$$

For the second step, the integrals in (4.1) are reformulated using running averages so that the problem is defined in the homogeneous domain $\bar{\Omega}$. More specifically, for any function f defined on Ω_c we introduce the approximation

$$\begin{aligned} \int_{\Omega_c} f \, \mathrm{d}\Omega &\approx \int_{\bar{\Omega}} f_\square \, \mathrm{d}\Omega, \\ f_\square &:= \frac{1}{|\Omega_\square|} \int_{\Omega_\square} f \, \mathrm{d}\Omega, \end{aligned} \tag{4.4}$$

where $\Omega_\square$ defines the Representative Volume Element (RVE), a sample of the microstructure of the material. The macro problem then becomes

$$\begin{aligned} \int_{\Omega_c} \frac{1}{|\Omega_\square|} \int_{\Omega_{\square,c}} \boldsymbol{\sigma}_c : \left[\delta \boldsymbol{u}_c^M \otimes \boldsymbol{\nabla}\right] \, \mathrm{d}\Omega \, \mathrm{d}\bar{\Omega} = \int_{\Omega_c} \frac{1}{|\Omega_\square|} \int_{\Omega_{\square,c}} \hat{\boldsymbol{b}} \cdot \delta \boldsymbol{u}_c^M \, \mathrm{d}\Omega \, \mathrm{d}\bar{\Omega} \\ + \int_{\Gamma_{ext}} \hat{\boldsymbol{t}} \cdot \delta \boldsymbol{u}_c^M \, \mathrm{d}\Gamma. \end{aligned} \tag{4.5}$$

Here, we have restricted to volumetric homogenisation. Hence, the surface integral over Γ_{ext} in (4.5) is not affected. Surface homogenisation has been treated, e.g., in the context of contact in [102]. In the next step, a suitable condition linking $\boldsymbol{u}^M$ and $\bar{\boldsymbol{u}}$ need to be defined in a process called *prolongation*. In the setting of first order computational homogenisation [49, 29], a Taylor series expansion of $\bar{\boldsymbol{u}}$ up to the first order term is used, i.e.,

$$\boldsymbol{u}^M = \bar{\boldsymbol{u}} \,|_{\bar{\boldsymbol{x}}} + \left[\bar{\boldsymbol{u}} \otimes \boldsymbol{\nabla}\right] |_{\bar{\boldsymbol{x}}} \cdot \left[\boldsymbol{x} - \bar{\boldsymbol{x}}\right], \tag{4.6}$$

where $\bar{\boldsymbol{x}} = \frac{1}{|\Omega_\square|} \int_{\Omega_\square} \boldsymbol{x} \, \mathrm{d}\Omega$ is the centre of the RVE. Inserting the prolongation condition in (4.5) and assuming that the field is sufficiently smooth at the boundary, i.e., that $\boldsymbol{u}_c^M \approx \bar{\boldsymbol{u}}$ on Γ_{ext}, we conclude that the macro problem becomes: Find $\bar{\boldsymbol{u}} \in \bar{\mathbb{U}}$ such that

$$\int_{\bar{\Omega}} \bar{\boldsymbol{\sigma}} : \left[\delta \bar{\boldsymbol{u}} \otimes \boldsymbol{\nabla}\right] \, \mathrm{d}\Omega = \int_{\Gamma_{ext}} \hat{\boldsymbol{t}} \cdot \delta \bar{\boldsymbol{u}} \, \mathrm{d}\Gamma + \int_{\bar{\Omega}} \bar{\boldsymbol{b}} \cdot \delta \bar{\boldsymbol{u}} + \bar{\boldsymbol{b}}^{(2)} : \left[\delta \bar{\boldsymbol{u}} \otimes \boldsymbol{\nabla}\right] \, \mathrm{d}\Omega \qquad \forall \delta \bar{\boldsymbol{u}} \in \bar{\mathbb{U}}^0, \tag{4.7}$$

where $\bar{\mathbb{U}}$ and $\bar{\mathbb{U}}^0$ are suitably defined trial and test spaces for the homogenised problem. The effective quantities are then identified as

$$\begin{aligned} \bar{\boldsymbol{\sigma}} &= \frac{1}{|\Omega_\square|} \int_{\Omega_{\square,c}} \boldsymbol{\sigma} \, \mathrm{d}\Omega, \\ \bar{\boldsymbol{b}} &= \frac{1}{|\Omega_\square|} \int_{\Omega_{\square,c}} \hat{\boldsymbol{b}} \, \mathrm{d}\Omega, \\ \bar{\boldsymbol{b}}^{(2)} &= \frac{1}{|\Omega_\square|} \int_{\Omega_{\square,c}} \hat{\boldsymbol{b}} \otimes \left[\boldsymbol{x} - \bar{\boldsymbol{x}}\right] \, \mathrm{d}\Omega, \end{aligned} \tag{4.8}$$

and can be computed from the solution of subscale problem. This process of averaging subscale variables to an effective macroscopic variable is called *homogenisation* or *micro-to-macro transition*. In the presented example, $\bar{\boldsymbol{\sigma}}$ and $\bar{\boldsymbol{b}}$ denote the effective stress and body force, respectively, while $\bar{\boldsymbol{b}}^{(2)}$ is a higher order term. Thus, for every macroscopic point $\bar{\boldsymbol{x}}$, the macroscopic fields (and gradients) can be imposed on the associated RVE via suitable boundary conditions. The RVE problem is then solved, and the subscale variables are averaged to produce a macroscopic effective variable. It is noteworthy that it is only the symmetric part of the macroscopic deformation gradient, $[\bar{\boldsymbol{u}} \otimes \boldsymbol{\nabla}]^{\mathrm{sym}}$, that affects the macroscopic stress tensor. Due to invariance under rigid body motion $\bar{\boldsymbol{u}}$ and $[\bar{\boldsymbol{u}} \otimes \boldsymbol{\nabla}]^{\mathrm{skw}}$ do not affect $\bar{\boldsymbol{\sigma}}$.

Although VCH was applied in this Section to concrete continuum, the method maintains generality when reinforcement is introduced. As an additional assumption, the body forces $\hat{\boldsymbol{b}}$ were neglected in **Papers A–D**. Even though only one macroscopic field $\bar{\boldsymbol{u}}$ was considered in this section, it is possible to include additional macroscopic variables, provided that appropriate prolongation conditions are defined. This approach is further illustrated in **Papers B** and **C**, where a macroscopic reinforcement slip field, $\bar{\boldsymbol{s}}$, is introduced.

4.3 Subscale boundary conditions

Equation (4.3) localised in RVE represents the subscale problem which needs to be solved in each macroscopic point $\bar{\boldsymbol{x}}$. However, in order to solve the problem, suitable boundary conditions need to be applied on the RVE. In order to fulfil the so-called Hill-Mandel macrohomogeneity condition [36], which ensures energy equivalence across the scales, the average strain coming from the subscale fluctuation must vanish, i.e.,

$$\frac{1}{|\Omega_\square|} \int_{\Omega_\square} \boldsymbol{u}^s \otimes \boldsymbol{\nabla} \, \mathrm{d}\Omega = 0. \tag{4.9}$$

Using Gauss theorem, one can also express this requirement as a boundary integral. Even though (4.9) can be satisfied in a number of ways, three types of boundary conditions are most commonly used in practice, cf. Figure 4.2.

First of all, *Dirichlet* boundary conditions postulate that the subscale fluctuation field vanishes at the boundary of the RVE, i.e., $\boldsymbol{u}^s = \boldsymbol{0}$ on $\Gamma_\square$. This implies that the total displacement field $\boldsymbol{u}$ on the boundary of the RVE is equal to the macroscopic part $\boldsymbol{u}^M$, which varies linearly along the boundary. Note that solving the boundary value problem gives rise to boundary tractions.

In contrast, the *Neumann* boundary conditions do not impose any requirements on the fluctuation $\boldsymbol{u}^s$. Instead, the macroscopic strain and the average strain in the RVE are equated explicitly, i.e., $[\bar{\boldsymbol{u}} \otimes \boldsymbol{\nabla}]^{\mathrm{sym}} = \frac{1}{|\Omega_\square|} \int_{\Omega_\square} (\boldsymbol{u} \otimes \boldsymbol{\nabla})^{\mathrm{sym}} \, \mathrm{d}\Omega$. This is equivalent to the statement that the boundary tractions are generated from a constant stress tensor, and are thus piecewise constant along the boundary on the RVE. In displacement control setting, the macroscopic and average strain equality is imposed weakly on the RVE, with the help of Lagrange multipliers.

For the third option, the *Periodic* boundary conditions posit that the average jump in the fluctuation field at the opposite boundaries of the RVE is zero. Additionally, it is required that the tractions at the opposite boundaries are anti-periodic, i.e., they have the same value but point in opposite direction. This constraint can be imposed either weakly [97, 98] or strongly, in which case a periodic mesh is required. As a result, the fluctuation field is equal at the opposite boundaries, cf. Figure 4.2.

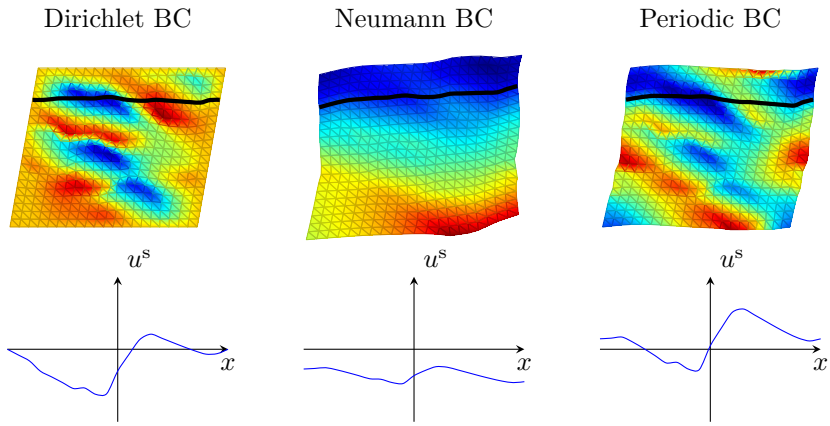

Figure 4.2: Subscale fluctuation fields, u^s, within the Representative Volume Element (RVE) for different types of boundary conditions resulting from the same macroscopic strain. The graphs show the fluctuation field along the black line indicated on the contour plots. Color scales differ between the RVEs.

It is noteworthy, that in case of a reinforced concrete structure, the VMS split is applied not only to the displacement field in concrete ($\boldsymbol{u}_\mathrm{c}$), but also to the displacement field in steel reinforcement ($\boldsymbol{u}_\mathrm{s}$). As a result, it is possible to apply different combinations of boundary conditions on a reinforced concrete RVE. The different Dirichlet/Neumann boundary condition combinations are studied in **Paper A** in detail. In **Papers B–D** Dirichlet boundary conditions are applied to both concrete and reinforcement, while periodic boundary conditions are used for both in **Paper E**. As already mentioned in the previous section, a macroscopic reinforcement slip field is also introduced and studied in this work. This field is imposed on the RVEs via Dirichlet boundary conditions in **Paper B**, while Neumann boundary conditions and Lagrange multipliers are used to impose the macroscopic slip field in **Paper C**.

4.4 FE^2 method

The FE^2 (Finite Element squared) method is the direct implementation of the concept presented in Sections 4.2 and 4.3. The internal algorithmic loop at a large-scale integration point, based on computational homogenisation, is schematically illustrated in Section 4.4. Macroscopically, the structure is represented with a homogeneous material with "effective" properties. The effective field and its gradient, computed at the integration points of large-scale finite elements, are imposed on the RVE via chosen boundary conditions. Upon solution of the RVE problem, the effective work conjugates are homogenised. The internal force vectors and macroscopic tangent stiffness matrix can then be computed for the macroscopic elements, allowing for nonlinear the analysis based on Newton's method. As a result, a nested FE algorithm is created. Even though FE^2 is computationally expensive, it is well suited for parallel computation, as all RVE problems are uncoupled and can be solved independently. FE^2 has been used to model e.g. diffusion phenomena [73], fibre-matrix composites [85], delamination in composites [35], and localisation phenomena [76, 104, 70, 100, 99, 13, 14].

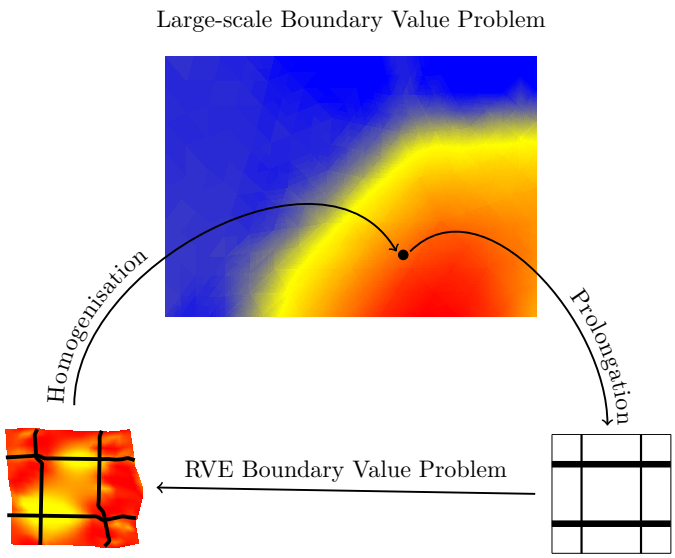

Figure 4.3: FE^2 scheme. At a given large-scale point, the effective fields are imposed on the RVE via chosen boundary conditions. The effective work conjugates are then computed from the solution of the RVE problem.

5 Multiscale models for reinforced concrete structures

5.1 Preliminaries

One of the advantages of the VCH is that upon introduction of a suitable prolongation scheme, the homogeneous macro problem is derived in a straight-forward way, and the associated scale transitions can be easily identified. Therefore, even though a three-dimensional solid formulation of the problem is used at the subscale, different macroscopic structural models can be obtained from VCH, depending on the employed prolongation. In this chapter the effective equations and the corresponding micro-to-macro transitions for a few different effective models, developed in course of this work, are presented along with the necessary assumptions. As the starting point, the VMS split of the displacement fields in concrete and steel is considered:

$$\boldsymbol{u}_{\mathrm{c}} = \boldsymbol{u}_{\mathrm{c}}^{M} + \boldsymbol{u}_{\mathrm{c}}^{s}, \qquad u_{\mathrm{s,l}} = u_{\mathrm{s,l}}^{M} + u_{\mathrm{s,l}}^{s}, \qquad \boldsymbol{u}_{\mathrm{s},\perp} = \boldsymbol{u}_{\mathrm{s},\perp}^{M} + \boldsymbol{u}_{\mathrm{s},\perp}^{s}. \tag{5.1}$$

5.2 Effective solid in plane stress

As a basis for derivation of this model, the fine-scale model for reinforced concrete described in Chapter 3 was simplified to two dimensions, cf. Figure 5.1. The thickness of the structure is constant and denoted t_{c} and is much smaller than the other dimensions. Hence, the plane stress state can be assumed. Furthermore, the body forces $\hat{\boldsymbol{b}}$ acting in the structure are neglected. Due to dimensionality reduction, unique longitudinal and transverse unit vectors $\boldsymbol{e}_{\mathrm{l}}$ and $\boldsymbol{e}_{\perp}$ can be defined for each reinforcement bar.

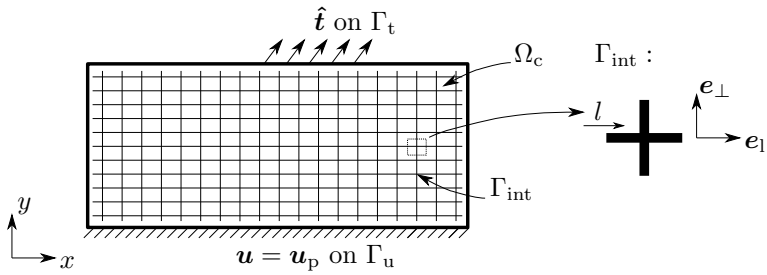

Figure 5.1: A two-dimensional reinforced concrete structure. For each reinforcement bar, longitudinal and transverse unit vectors $\boldsymbol{e}_{\mathrm{l}}$ and $\boldsymbol{e}_{\perp}$ are defined.

The unknown displacement fields are then decomposed into longitudinal and transverse components as

$$\begin{aligned} \boldsymbol{u}_{\mathrm{s,l}} &= u_{\mathrm{s,l}}\boldsymbol{e}_{\mathrm{l}}, \qquad \boldsymbol{u}_{\mathrm{c,l}} = u_{\mathrm{c,l}}\boldsymbol{e}_{\mathrm{l}}, \\ \boldsymbol{u}_{\mathrm{s},\perp} &= u_{\mathrm{s},\perp}\boldsymbol{e}_{\perp}, \quad \boldsymbol{u}_{\mathrm{c},\perp} = u_{\mathrm{c},\perp}\boldsymbol{e}_{\perp}. \end{aligned} \tag{5.2}$$

Next, the prolongation conditions linking the macroscopic parts of the fields with

the homogeneous smooth field $\bar{\boldsymbol{u}} = [\bar{u}\ \bar{v}]^{\mathrm{T}}$ are formulated using the usual first order homogenisation as:

$$\begin{aligned} \boldsymbol{u}_{\mathrm{c}}^{M} &= \bar{\boldsymbol{u}}\,|_{\bar{x}} + [\bar{\boldsymbol{u}} \otimes \boldsymbol{\nabla}]\,|_{\bar{x}} \cdot [\boldsymbol{x} - \bar{\boldsymbol{x}}]\,, \\ u_{\mathrm{s,l}}^{M} &= \boldsymbol{e}_{\mathrm{l}} \cdot \boldsymbol{u}_{\mathrm{c}}^{M} = \boldsymbol{e}_{\mathrm{l}} \cdot \bar{\boldsymbol{u}}\,|_{\bar{x}} + \boldsymbol{e}_{\mathrm{l}} \cdot [\bar{\boldsymbol{u}} \otimes \boldsymbol{\nabla}]\,|_{\bar{x}} \cdot [\boldsymbol{x} - \bar{\boldsymbol{x}}]\,, \\ u_{\mathrm{s},\perp}^{M} &= \boldsymbol{e}_{\perp} \cdot \boldsymbol{u}_{\mathrm{c}}^{M} = \boldsymbol{e}_{\perp} \cdot \bar{\boldsymbol{u}}\,|_{\bar{x}} + \boldsymbol{e}_{\perp} \cdot [\bar{\boldsymbol{u}} \otimes \boldsymbol{\nabla}]\,|_{\bar{x}} \cdot [\boldsymbol{x} - \bar{\boldsymbol{x}}]\,. \end{aligned} \tag{5.3}$$

It is noteworthy, that the macroscopic part of the displacement field in steel $\boldsymbol{u}_{\mathrm{s}}^{M}$ derives entirely from the macroscopic displacement field in concrete $\boldsymbol{u}_{\mathrm{c}}^{M}$. As a result, the reinforcement slip is allowed to exist only at the RVE level.

Upon further derivation, the large-scale problem in this model becomes: Find $\bar{\boldsymbol{u}} \in \bar{\mathbb{U}}$ such that

$$\int_{\bar{\Omega}} \bar{\boldsymbol{\sigma}} : [\delta\bar{\boldsymbol{u}} \otimes \boldsymbol{\nabla}]\ \mathrm{d}\Omega = \int_{\Gamma_{\mathrm{ext}}} t_{\mathrm{c}}\hat{\boldsymbol{t}} \cdot \delta\bar{\boldsymbol{u}}\ \mathrm{d}\Gamma \qquad \forall\ \delta\bar{\boldsymbol{u}} \in \bar{\mathbb{U}}^{0}, \tag{5.4}$$

where $\bar{\mathbb{U}}$ and $\bar{\mathbb{U}}^{0}$ are suitably defined trial and test spaces. From the result, the *effective stress* $\bar{\boldsymbol{\sigma}}$ is identified as

$$\bar{\boldsymbol{\sigma}} = \frac{1}{|\Omega_{\square}|}\left\{ \int_{\Omega_{\square,\mathrm{c}}} t_{\mathrm{c}}\boldsymbol{\sigma}_{\mathrm{c}}\ \mathrm{d}\Omega + \int_{\Gamma_{\square,\mathrm{int}}} N_{\mathrm{s}}\boldsymbol{e}_{\mathrm{l}} \otimes \boldsymbol{e}_{\mathrm{l}} \right\}, \tag{5.5}$$

with $\boldsymbol{\sigma}$ being the stress tensor in concrete and N_{s} being the normal force in the reinforcement. More detailed derivation of this model can be found in **Paper A**. In summary, for a given macroscopic strain $\bar{\boldsymbol{\varepsilon}} = [\bar{\boldsymbol{u}} \otimes \boldsymbol{\nabla}]^{\mathrm{sym}}$ it is possible to compute the work conjugated effective membrane stress tensor $\bar{\boldsymbol{\sigma}}$ from computational homogenisation of the RVE response.

5.3 Effective Euler-Bernoulli beam

In order to upscale the subscale structure to an effective Euler-Bernoulli beam element, the three-dimensional fully-resolved representation is used as a basis, cf. Figure 5.2.

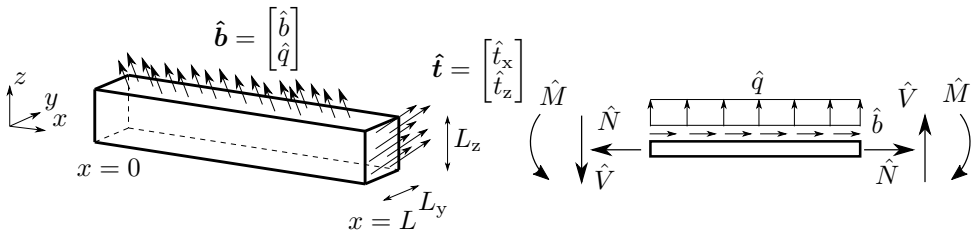

(a) Fully-resolved representation (b) Macroscopic simplification

Figure 5.2: Fully-resolved representation (a) and the macroscopic model (b) for a beam structure. Tractions $\hat{\boldsymbol{t}}$ at beam ends give rise to end forces $\hat{N}$, $\hat{V}$ and $\hat{M}$.

Since the macroscopic beam is defined in xz-plane, only x- and z-components of the total displacement field are considered to vary at the macroscale, and the y-component

is assumed to live only at the subscale. Consequently, the VMS split for the concrete displacement is expressed as

$$\boldsymbol{u}_{\mathrm{c}} = \boldsymbol{u}_{\mathrm{c}}^{M} + \boldsymbol{u}_{\mathrm{c}}^{\mathrm{s}} = \begin{bmatrix} u_{\mathrm{c}}^{M} \\ 0 \\ w_{\mathrm{c}}^{M} \end{bmatrix} + \begin{bmatrix} u_{\mathrm{c}}^{s} \\ v_{\mathrm{c}}^{s} \\ w_{\mathrm{c}}^{s} \end{bmatrix}. \tag{5.6}$$

Next, a macroscopic field $\bar{\boldsymbol{u}} = [\bar{u}\ \bar{w}]$ is considered. Employing the Euler-Bernoulli beam model kinematics, the following prolongation conditions are established:

$$\begin{aligned} u_{\mathrm{c}}^{M} &= \bar{u}\,|_{\bar{x}} - z\frac{\partial \bar{w}}{\partial x}\bigg|_{\bar{x}} + \frac{\partial \bar{u}}{\partial x}\bigg|_{\bar{x}} [x-\bar{x}] - z\frac{\partial^2 \bar{w}}{\partial x^2}\bigg|_{\bar{x}} [x-\bar{x}]\,, \\ w_{\mathrm{c}}^{M} &= \bar{w}\,|_{\bar{x}} + \frac{\partial \bar{w}}{\partial x}\bigg|_{\bar{x}} [x-\bar{x}]\,, \\ u_{\mathrm{s,l}}^{M} &= \boldsymbol{e}_{\mathrm{l}} \cdot \boldsymbol{u}_{\mathrm{c}}^{M} = e_{\mathrm{lx}} u_{\mathrm{c}}^{M} + e_{\mathrm{lz}} w_{\mathrm{c}}^{M}, \\ \boldsymbol{u}_{\mathrm{s},\perp}^{M} &= \boldsymbol{I}_{\perp} \cdot \boldsymbol{u}_{\mathrm{c}}^{M}. \end{aligned} \tag{5.7}$$

In the above, e_{lx} and e_{lz} denote the x- and z-components, respectively, of the longitudinal unit vector $\boldsymbol{e}_{\mathrm{l}}$ associated with the reinforcement bar. Since the macroscopic part of the displacement field in steel $\boldsymbol{u}_{\mathrm{s}}^{M}$ derives entirely from the macroscopic displacement field in concrete $\boldsymbol{u}_{\mathrm{c}}^{M}$, only subscale variation of the reinforcement slip is considered. The large-scale problem for the effective Euler-Bernoulli beam model is obtained as: Find $\bar{u}, \bar{w} \in \bar{\mathbb{U}} \times \bar{\mathbb{W}}$ such that

$$\begin{aligned} \int_0^L \bar{N} \frac{\partial \delta \bar{u}}{\partial x}\ \mathrm{d}x &= \left[\hat{N} \delta \bar{u}\right]_0^L + \int_0^L \hat{b} \delta \bar{u} \mathrm{d}x && \forall\ \delta \bar{u} \in \bar{\mathbb{U}}^0, \\ \int_0^L \bar{M} \frac{\partial^2 \delta \bar{w}}{\partial x^2}\ \mathrm{d}x &= \left[\hat{M} \frac{\partial \delta \bar{w}}{\partial x}\right]_0^L - \left[\hat{V} \delta \bar{w}\right]_0^L - \int_0^L \hat{q} \delta \bar{w}\ \mathrm{d}x && \forall\ \delta \bar{w} \in \bar{\mathbb{W}}^0, \end{aligned} \tag{5.8}$$

with the suitable trial and test spaces. The end forces $\hat{N}$,$\hat{V}$, and $\hat{M}$ introduced in (5.8), which represent the prescribed boundary data, constitute natural boundary conditions. As the result of VCH, the *effective normal force* $\bar{N}$ and *effective bending moment* $\bar{M}$ become

$$\begin{aligned} \bar{N} &= \frac{1}{|L_{\square}|} \left\{ \int_{\Omega_{\square,\mathrm{c}}} \sigma_{\mathrm{xx}}\ \mathrm{d}\Omega + \int_{\Gamma_{\square,\mathrm{int}}} N_{\mathrm{s}} e_{\mathrm{lx}}^2\ \mathrm{d}\Gamma \right\}, \\ \bar{M} &= \frac{1}{|L_{\square}|} \left\{ \int_{\Omega_{\square,\mathrm{c}}} z\sigma_{\mathrm{xx}} + \sigma_{\mathrm{xz}} [x-\bar{x}]\ \mathrm{d}\Omega + \right. \\ &\qquad \left. \int_{\Gamma_{\square,\mathrm{int}}} N_{\mathrm{s}} \left(z e_{\mathrm{lx}}^2 + e_{\mathrm{lz}} e_{\mathrm{lx}} [x-\bar{x}] \right) + 2 e_{\mathrm{lz}} \sum_{i=1}^{2} M_{\mathrm{s,i}} e_{\perp,\mathrm{i,x}} e_{\mathrm{lx}}\ \mathrm{d}\Gamma \right\}, \end{aligned}$$

where σ_{xx} and σ_{xz} are the xx- and xz-components of the concrete stress tensor, and where N_{s} is the normal force in the reinforcement bar. Bending moments $M_{\mathrm{s,i}}$ and unit vectors

$\boldsymbol{e}_{\perp,\mathrm{i}}$ pertain to transverse direction i of the rebar, cf. Figure 3.1. It is also noteworthy that the previously used volume of the RVE, $\Omega_\square$, has been replaced by the length of the unit cell in x-direction, $L_\square$. More detailed derivation of this model can be found in **Paper E**. In summary, for a given macroscopic axial strain $\bar{\varepsilon} = \partial\bar{u}/\partial x$ and macroscopic curvature $\bar{\kappa} = \partial^2\bar{w}/\partial x^2$ it is possible to compute the work conjugated effective normal force $\bar{N}$ and bending moment $\bar{M}$ from computational homogenisation of the response of the RVE.

5.4 Effective Kirchhoff-Love plate

As a basis for upscaling to an effective plate model, a three-dimensional fully-resolved representation is used, cf. Figure 5.3.

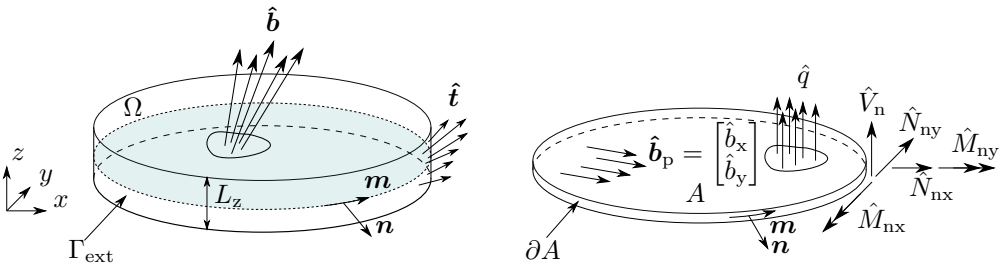

(a) Fully-resolved representation (b) Macroscopic simplification

Figure 5.3: Fully-resolved representation (a) and the macroscopic model (b) for a plate structure. Tractions $\hat{\boldsymbol{t}}$ at the external boundary Γ_ext give rise to membrane forces $\hat{N}_\mathrm{nx}, \hat{N}_\mathrm{ny}$, shear force $\hat{V}_\mathrm{n}$, and bending moments $\hat{M}_\mathrm{nx}, \hat{M}_\mathrm{ny}$ at a point on external boundary ∂A with normal and tangential unit vectors $\boldsymbol{n}$ and $\boldsymbol{m}$, respectively.

Since the plate is defined in the xy-plane, the coordinate vector $\boldsymbol{x}$ along with the reinforcement unit vectors $\boldsymbol{e}_\mathrm{l}$ and $\boldsymbol{e}_{\perp,\mathrm{i}}$ are split into in-plane and out-of-plane components, i.e., $\boldsymbol{x} = [\boldsymbol{x}_\mathrm{p}\ z]^\mathrm{T}$, where the $\boldsymbol{x}_\mathrm{p} = [x\ y]^\mathrm{T}$. Similarly, $\boldsymbol{e}_\mathrm{l} = [\boldsymbol{e}_\mathrm{lp}\ e_\mathrm{lz}]^\mathrm{T}$ and $\boldsymbol{e}_{\perp,\mathrm{i}} = [\boldsymbol{e}_{\perp,\mathrm{i,p}}\ e_{\perp,\mathrm{i,z}}]^\mathrm{T}$ with the membrane components $\boldsymbol{e}_\mathrm{lp} = [e_\mathrm{lx}\ e_\mathrm{ly}]^\mathrm{T}$ and $\boldsymbol{e}_{\perp,\mathrm{i,p}} = [e_{\perp,\mathrm{i,x}}\ e_{\perp,\mathrm{i,y}}]^\mathrm{T}$, respectively. Similarly, the gradient operator $\boldsymbol{\nabla}_\mathrm{p}$ defines the gradient with respect to the in-plane coordinates.

Next, a macroscopic field $\bar{\boldsymbol{u}} = [\bar{\boldsymbol{u}}_\mathrm{p}\ \bar{w}]^\mathrm{T}$ is considered, where $\bar{\boldsymbol{u}}_\mathrm{p}$ denotes the membrane components of the fields, i.e. $\bar{\boldsymbol{u}}_\mathrm{p} = [\bar{u}\ \bar{v}]^\mathrm{T}$. Since the Kirchhoff-Love model kinematics is simply a two-dimensional extension of the Euler-Bernoulli model, the prolongation conditions can be expressed as

$$
\begin{aligned}
\boldsymbol{u}_\mathrm{c}^M &= \begin{bmatrix} \bar{\boldsymbol{u}}_\mathrm{p}\,|_{\bar{\boldsymbol{x}}_\mathrm{p}} - z\boldsymbol{\nabla}_\mathrm{p}\bar{w}\,|_{\bar{\boldsymbol{x}}_\mathrm{p}} + [\bar{\boldsymbol{u}}_\mathrm{p}\otimes\boldsymbol{\nabla}_\mathrm{p}]\,|_{\bar{\boldsymbol{x}}_\mathrm{p}}\cdot[\boldsymbol{x}_\mathrm{p}-\bar{\boldsymbol{x}}_\mathrm{p}] - z\,[\boldsymbol{\nabla}_\mathrm{p}\bar{w}\otimes\boldsymbol{\nabla}_\mathrm{p}]\,|_{\bar{\boldsymbol{x}}_\mathrm{p}}\cdot[\boldsymbol{x}_\mathrm{p}-\bar{\boldsymbol{x}}_\mathrm{p}] \\ \bar{w}\,|_{\bar{\boldsymbol{x}}_\mathrm{p}} + \boldsymbol{\nabla}_\mathrm{p}\bar{w}\,|_{\bar{\boldsymbol{x}}_\mathrm{p}}\cdot[\boldsymbol{x}_\mathrm{p}-\bar{\boldsymbol{x}}_\mathrm{p}] \end{bmatrix}, \\
u_{\mathrm{s,l}}^M &= \boldsymbol{e}_\mathrm{l}\cdot\boldsymbol{u}_\mathrm{c}^M, \\
\boldsymbol{u}_{\mathrm{s},\perp}^M &= \boldsymbol{I}_\perp\cdot\boldsymbol{u}_\mathrm{c}^M.
\end{aligned}
\tag{5.9}
$$

Similar to previous models, the macroscopic part of the displacement field in steel $\boldsymbol{u}_{\mathrm{s}}^{M}$ derives entirely from the concrete displacement. Hence, the reinforcement slip is allowed to vary only at the RVE level. For simplicity, we define the boundary membrane normal forces and bending moments with component representation

$$\hat{\boldsymbol{N}}_{\mathrm{p}} = \begin{bmatrix} \hat{N}_{\mathrm{xx}} & \hat{N}_{\mathrm{xy}} \\ \hat{N}_{\mathrm{yx}} & \hat{N}_{\mathrm{yy}} \end{bmatrix} \qquad \text{and} \qquad \hat{\boldsymbol{M}}_{\mathrm{p}} = \begin{bmatrix} \hat{M}_{\mathrm{xx}} & \hat{M}_{\mathrm{xy}} \\ \hat{M}_{\mathrm{yx}} & \hat{M}_{\mathrm{yy}} \end{bmatrix}. \tag{5.10}$$

Following the derivation, the large-scale problem for the effective Kirchhoff-Love plate model can be obtained as: Find $\bar{\boldsymbol{u}}_{\mathrm{p}}, \bar{w} \in \bar{\mathbb{U}} \times \bar{\mathbb{W}}$ such that

$$\begin{aligned} \int_A \bar{\boldsymbol{N}} : [\delta\bar{\boldsymbol{u}}_{\mathrm{p}} \otimes \boldsymbol{\nabla}_{\mathrm{p}}] \ \mathrm{d}A &= \int_{\partial A} \hat{\boldsymbol{N}}_{\mathrm{p,n}} \cdot \delta\bar{\boldsymbol{u}}_{\mathrm{p}} \ \mathrm{d}\Gamma + \int_A \hat{\boldsymbol{b}}_{\mathrm{p}} \cdot \delta\bar{\boldsymbol{u}}_{\mathrm{p}} \ \mathrm{d}A \qquad \forall\ \delta\bar{\boldsymbol{u}}_{\mathrm{p}} \in \bar{\mathbb{U}}^0, \\ \int_A \bar{\boldsymbol{M}} : [\boldsymbol{\nabla}_{\mathrm{p}}\delta\bar{w} \otimes \boldsymbol{\nabla}_{\mathrm{p}}] \ \mathrm{d}A &= \int_{\partial A} \hat{M}_{\mathrm{p,n}} \frac{\partial \delta\bar{w}}{\partial n} - \hat{V}_{\mathrm{n}}^{\mathrm{K}} \delta\bar{w} \ \mathrm{d}\Gamma - \int_A \hat{q}\delta\bar{w} \ \mathrm{d}A \quad \forall\ \delta\bar{w} \in \bar{\mathbb{W}}^0, \end{aligned} \tag{5.11}$$

with the suitable trial and test spaces. The boundary membrane forces $\hat{\boldsymbol{N}}_{\mathrm{p,n}}$, boundary Kirchhoff force $\hat{V}_{\mathrm{n}}^{\mathrm{K}}$ and boundary moment $\hat{M}_{\mathrm{p,n}}$ present on the right hand side of (5.11) are defined as

$$\hat{\boldsymbol{N}}_{\mathrm{p,n}} = \hat{\boldsymbol{N}}_{\mathrm{p}} \cdot \boldsymbol{n}, \quad \hat{V}_{\mathrm{n}}^{\mathrm{K}} = \hat{V}_{\mathrm{n}} + \frac{\partial}{\partial m}\left(\hat{\boldsymbol{M}}_{\mathrm{p}} : [\boldsymbol{n} \otimes \boldsymbol{m}]\right), \quad \hat{M}_{\mathrm{p,n}} = \hat{\boldsymbol{M}}_{\mathrm{p}} : [\boldsymbol{n} \otimes \boldsymbol{n}], \tag{5.12}$$

and denote the prescribed boundary data or reaction forces. From the results of VCH, the *effective membrane forces* $\bar{\boldsymbol{N}}$ and the *effective bending moments* $\bar{\boldsymbol{M}}$ are identified as

$$\begin{aligned} \bar{\boldsymbol{N}} &= \frac{1}{|A_{\square}|}\left\{\int_{\Omega_{\square,\mathrm{c}}} \boldsymbol{\sigma}_{\mathrm{p}} \ \mathrm{d}\Omega + \int_{\Gamma_{\square,\mathrm{int}}} N_{\mathrm{s}} \boldsymbol{e}_{\mathrm{lp}} \otimes \boldsymbol{e}_{\mathrm{lp}} \ \mathrm{d}\Gamma\right\}, \\ \bar{\boldsymbol{M}} &= \frac{1}{|A_{\square}|}\left\{\int_{\Omega_{\square,\mathrm{c}}} z\boldsymbol{\sigma}_{\mathrm{p}} + \boldsymbol{\sigma}_{\mathrm{z}} \otimes [\boldsymbol{x}_{\mathrm{p}} - \bar{\boldsymbol{x}}_{\mathrm{p}}] \ \mathrm{d}\Omega + \right. \\ &\qquad \left. \int_{\Gamma_{\square,\mathrm{int}}} N_{\mathrm{s}}\left(z\boldsymbol{e}_{\mathrm{lp}} \otimes \boldsymbol{e}_{\mathrm{lp}} + e_{\mathrm{lz}}\boldsymbol{e}_{\mathrm{lp}} \otimes [\boldsymbol{x}_{\mathrm{p}} - \bar{\boldsymbol{x}}_{\mathrm{p}}]\right) + 2e_{\mathrm{lz}} \sum_{i=1}^{2} M_{\mathrm{s,i}} \boldsymbol{e}_{\perp,\mathrm{i,p}} \otimes \boldsymbol{e}_{\mathrm{lp}} \ \mathrm{d}\Gamma \right\}, \end{aligned} \tag{5.13}$$

where $\boldsymbol{\sigma}_{\mathrm{p}}$ and $\boldsymbol{\sigma}_{\mathrm{z}}$ contain the in-plane and the out-of-plane components of the concrete stress tensor $\boldsymbol{\sigma}_{\mathrm{c}}$, i.e.,

$$\boldsymbol{\sigma}_{\mathrm{p}} = \begin{bmatrix} \sigma_{\mathrm{xx}} & \sigma_{\mathrm{xy}} \\ \sigma_{\mathrm{yx}} & \sigma_{\mathrm{yy}} \end{bmatrix} \qquad \text{and} \qquad \boldsymbol{\sigma}_{\mathrm{z}} = \begin{bmatrix} \sigma_{\mathrm{xz}} \\ \sigma_{\mathrm{yz}} \end{bmatrix}. \tag{5.14}$$

It is noteworthy that the previously used volume of the RVE, $\Omega_{\square}$ has been replaced by the area of the unit cell in xy-plane, $A_{\square}$. More detailed derivation of this model can be found in **Paper E**. In summary, for a given macroscopic membrane strain tensor $\bar{\boldsymbol{\varepsilon}}_{\mathrm{p}} = [\bar{\boldsymbol{u}}_{\mathrm{p}} \otimes \boldsymbol{\nabla}_{\mathrm{p}}]^{\mathrm{sym}}$ and a macroscopic curvature tensor $\bar{\boldsymbol{\kappa}} = [\boldsymbol{\nabla}_{\mathrm{p}}\bar{w} \otimes \boldsymbol{\nabla}_{\mathrm{p}}]$ it is possible to compute the work conjugated effective membrane forces $\bar{\boldsymbol{N}}$ and bending moments $\bar{\boldsymbol{M}}$ from computational homogenisation of the response of the RVE.

5.5 Macroscopic reinforcement slip

In order to allow for the transfer of reinforcement slip across macroscopic elements, the model presented in Section 5.2 is subsequently enriched by a macroscopic reinforcement slip field, $\bar{\boldsymbol{s}} = [\bar{s}_\mathrm{x}\ \bar{s}_\mathrm{y}]^\mathrm{T}$, representing the displacement of the reinforcement grid relative to concrete, cf. Figure 5.4.

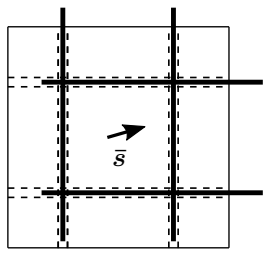

Figure 5.4: Interpretation of the macroscopic reinforcement slip field.

More specifically, the new effective field is introduced into the model by modification of the prolongation condition for the longitudinal displacement in steel:

$$\begin{aligned} \boldsymbol{u}_\mathrm{c}^M &= \bar{\boldsymbol{u}}\,|_{\bar{x}} + [\bar{\boldsymbol{u}} \otimes \boldsymbol{\nabla}]\,|_{\bar{x}} \cdot [\boldsymbol{x} - \bar{\boldsymbol{x}}]\,, \\ u_{\mathrm{s,l}}^M &= \boldsymbol{e}_\mathrm{l} \cdot \boldsymbol{u}_\mathrm{c}^M + \boldsymbol{e}_\mathrm{l} \cdot \bar{\boldsymbol{s}}\,|_{\bar{x}} + \boldsymbol{e}_\mathrm{l} \cdot [\bar{\boldsymbol{s}} \otimes \boldsymbol{\nabla}]\,|_{\bar{x}} \cdot [\boldsymbol{x} - \bar{\boldsymbol{x}}]\,, \\ u_{\mathrm{s},\perp}^M &= \boldsymbol{e}_\perp \cdot \boldsymbol{u}_\mathrm{c}^M. \end{aligned} \tag{5.15}$$

Upon further derivation, the macroscopic problem in this model becomes: Find $\bar{\boldsymbol{u}}, \bar{\boldsymbol{s}} \in \bar{\mathbb{U}} \times \bar{\mathbb{S}}$ such that

$$\begin{aligned} \int_{\bar{\Omega}} \bar{\boldsymbol{\sigma}} : [\delta\bar{\boldsymbol{u}} \otimes \boldsymbol{\nabla}]\ \mathrm{d}\Omega &= \int_{\Gamma_\mathrm{ext}} t_\mathrm{c}\hat{\boldsymbol{t}} \cdot \delta\bar{\boldsymbol{u}}\ \mathrm{d}\Gamma \qquad \forall\ \delta\bar{\boldsymbol{u}} \in \bar{\mathbb{U}}^0, \\ \int_{\bar{\Omega}} \bar{\boldsymbol{\tau}}_\mathrm{b} \cdot \delta\bar{\boldsymbol{s}} + \bar{\boldsymbol{\sigma}}_\mathrm{s} : [\delta\bar{\boldsymbol{s}} \otimes \boldsymbol{\nabla}]\ \mathrm{d}\Omega &= 0 \qquad \forall\ \delta\bar{\boldsymbol{s}} \in \bar{\mathbb{S}}, \end{aligned} \tag{5.16}$$

where $\bar{\mathbb{U}}$, $\bar{\mathbb{U}}^0$ and $\bar{\mathbb{S}}$ are suitably defined trial and test spaces. From the result of VCH, the *effective stress* $\bar{\boldsymbol{\sigma}}$, *effective transfer stress* $\bar{\boldsymbol{\tau}}_\mathrm{b}$ and the *effective reinforcement stress* $\bar{\boldsymbol{\sigma}}_\mathrm{s}$ are identified as

$$\begin{aligned} \bar{\boldsymbol{\sigma}} &= \frac{1}{|\Omega_\square|} \left\{ \int_{\Omega_{\square,\mathrm{c}}} t_\mathrm{c}\boldsymbol{\sigma}\ \mathrm{d}\Omega + \int_{\Gamma_{\square,\mathrm{int}}} N_\mathrm{s}\boldsymbol{e}_\mathrm{l} \otimes \boldsymbol{e}_\mathrm{l} \right\}, \\ \bar{\boldsymbol{\tau}}_\mathrm{b} &= \frac{1}{|\Omega_\square|} \int_{\Gamma_{\square,\mathrm{int}}} S_\mathrm{s} t_\Gamma \boldsymbol{e}_\mathrm{l}\ \mathrm{d}\Gamma, \\ \bar{\boldsymbol{\sigma}}_\mathrm{s} &= \frac{1}{|\Omega_\square|} \int_{\Gamma_{\square,\mathrm{int}}} S_\mathrm{s} t_\Gamma \boldsymbol{e}_\mathrm{l} \otimes [\boldsymbol{x} - \bar{\boldsymbol{x}}] + N_\mathrm{s}\boldsymbol{e}_\mathrm{l} \otimes \boldsymbol{e}_\mathrm{l}\ \mathrm{d}\Gamma, \end{aligned} \tag{5.17}$$

with $\boldsymbol{\sigma}$ being the stress tensor in concrete, N_s being the normal force in the reinforcement, S_s denoting the perimeter of the rebar, and t_Γ representing the bond stress in the

steel/concrete interface. Note that in order to solve the problem (5.16), a custom finite element implementation allowing for discretisation of two fields is needed. More details regarding the derivation of the multiscale model and numerical implementation can be found in **Paper B**. In summary, for a given macroscopic strain $\bar{\boldsymbol{\varepsilon}} = [\bar{\boldsymbol{u}} \otimes \boldsymbol{\nabla}]^{\mathrm{sym}}$, macroscopic slip $\bar{\boldsymbol{s}}$ and a macroscopic slip gradient $\bar{\boldsymbol{g}} = [\bar{\boldsymbol{s}} \otimes \boldsymbol{\nabla}]$, it is possible to compute the work conjugated effective membrane stress tensor $\bar{\boldsymbol{\sigma}}$, effective transfer stress $\bar{\boldsymbol{\tau}}_{\mathrm{b}}$, and the effective reinforcement stress $\bar{\boldsymbol{\sigma}}_{\mathrm{s}}$ from computational homogenisation of the RVE response.

6 Summary of appended papers

Paper A: **Two-scale finite element modelling of reinforced concrete structures: effective response and subscale fracture development**
In **Paper A**, Variationally Consistent Homogenisation is used to derive a two-scale model for reinforced concrete, whereby a two-dimensional reinforced concrete structure is upscaled to effective solid in plane stress, cf. Section 5.2. The displacement field in steel derives explicitly from the concrete displacement, and thus the reinforcement slip lives only at the subscale. For the RVE, Dirichlet and Neumann boundary conditions are considered for the concrete and steel reinforcement, respectively. Therefore, four combinations of subscale boundary conditions are studied: Dirichlet-Dirichlet (DD), Dirichlet-Neumann (DN), Neumann-Dirichlet (ND) and Neumann-Neumann (NN), see Figure 6.1.

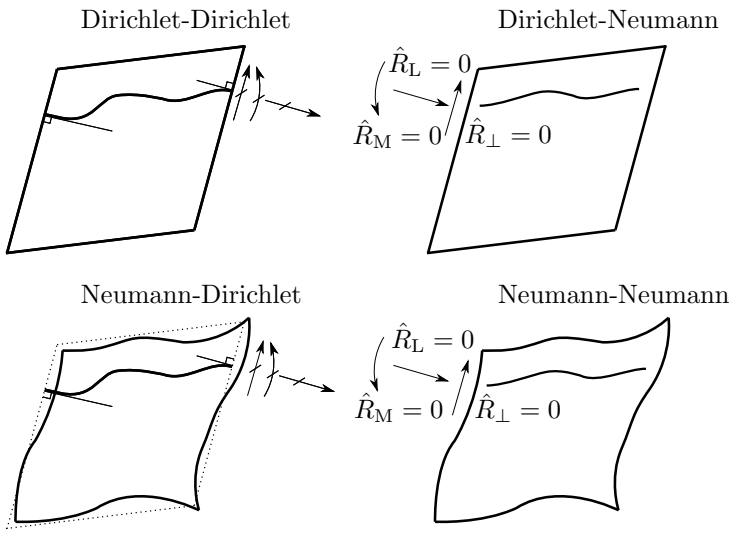

Figure 6.1: Combinations of subscale boundary conditions used in **Paper A**.

The developed multiscale algorithm is then used in analysis of a deep beam in four-point bending and the results are compared with the single-scale solution. The main results of **Paper A** can be summarised as follows:

- DD and NN boundary conditions provided respective upper and lower bounds on the effective elastic stiffness of the material, see Figure 6.2.
- Excessive softening in the RVE was observed for the DN and NN combinations.
- DD and ND boundary conditions simulated the global structural behaviour well, but the RVE response was found to be more reliable and consistent for the DD boundary conditions.
- Maximum crack widths were underestimated by the DD boundary conditions, see Figure 6.3.

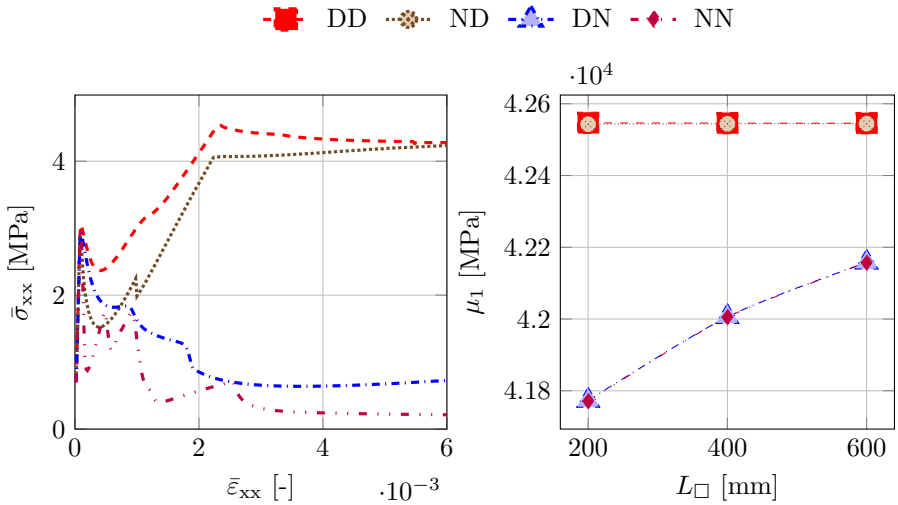

Figure 6.2: Homogenised stress-strain response of the RVEs under uniaxial tension (left). Influence of the RVE size, $L_\square$, on the largest eigenvalue of the elastic stiffness tensor, μ_1. (right)

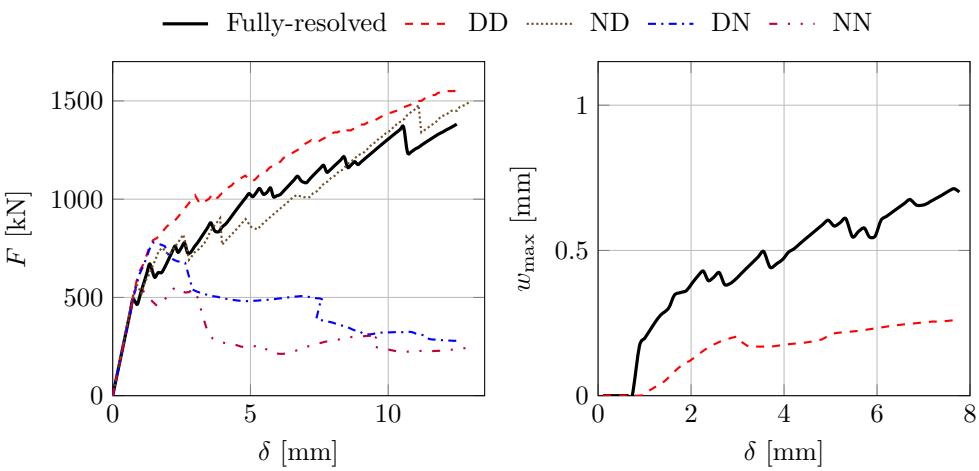

Figure 6.3: External load (left), F, and maximum crack width (right), $w_{\max}$, versus mid-span deflection, δ, for two-scale analyses using a single-sized RVE compared with fully-resolved analysis.

Paper B: **A multiscale model for reinforced concrete with macroscopic variation of reinforcement slip**
In **Paper B**, the multiscale model from **Paper A** is enriched by a macroscopic reinforcement slip variable, $\bar{\boldsymbol{s}}$, representing the deformation of the reinforcement grid relative to concrete, cf. Section 5.5. For the subscale RVE problem, Dirichlet boundary conditions were considered for both effective fields. More specifically, the previously studied DD boundary condition is used to impose the macroscopic displacement gradient $[\bar{\boldsymbol{u}} \otimes \boldsymbol{\nabla}]^{\mathrm{sym}}$ on the unit cell. On top of that, the macroscopic slip $\bar{\boldsymbol{s}}$ and its gradient $[\bar{\boldsymbol{s}} \otimes \boldsymbol{\nabla}]$ are imposed strongly on the boundary of the RVE, i.e., at the endpoints of the rebars.

For the numerical simulations, a reinforcement pull-through test is simulated on the RVEs. Furthermore, the deep beam from **Paper A** is analysed with the newly developed multiscale formulation. The main results of **Paper B** can be summarised as follows:

- Incorporation of the macroscopic reinforcement slip variable resulted in localisation of the effective strain at the macroscale, see Figure 6.4.
- Due to scale mixing in the enriched two-scale models, not only RVE size, but also the macroscopic mesh size influenced the resolution of the effective strain in the beam.
- Globally, the effective force–deflection response was not significantly influenced by the enrichment, see Figure 6.5. Moreover, the global response was not very sensitive to the macroscopic mesh size and the RVE size.
- The enriched two-scale models predicted larger crack widths compared to **Paper A**, but the single-scale results were still underestimated by most of the multiscale analyses, cf. Figure 6.5.
- The effective bond-stress versus effective slip relations obtained from the pull-through tests were RVE-size dependent, see Figure 6.6. The input bond-slip law was recovered only for small unit cells, which signifies that the physical interpretation of the macroscopic slip depends on the size of the unit cell.

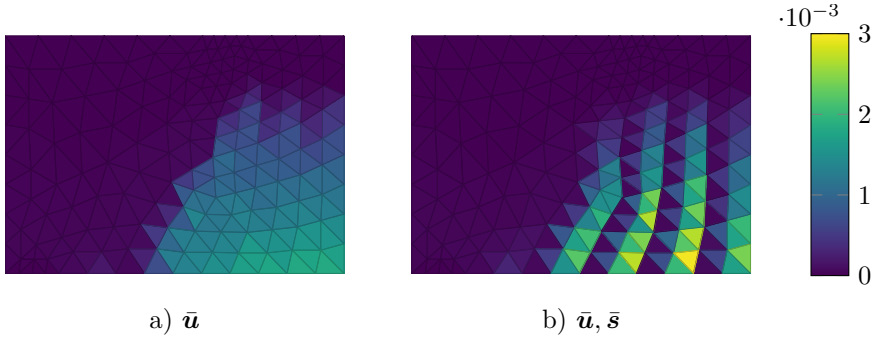

a) $\bar{\boldsymbol{u}}$ b) $\bar{\boldsymbol{u}}, \bar{\boldsymbol{s}}$

Figure 6.4: First principal strain, $\bar{\varepsilon}_1$, in the deep beam computed at the same large-scale deformation with the two-scale model without (a) and with (b) macroscopic reinforcement slip field.

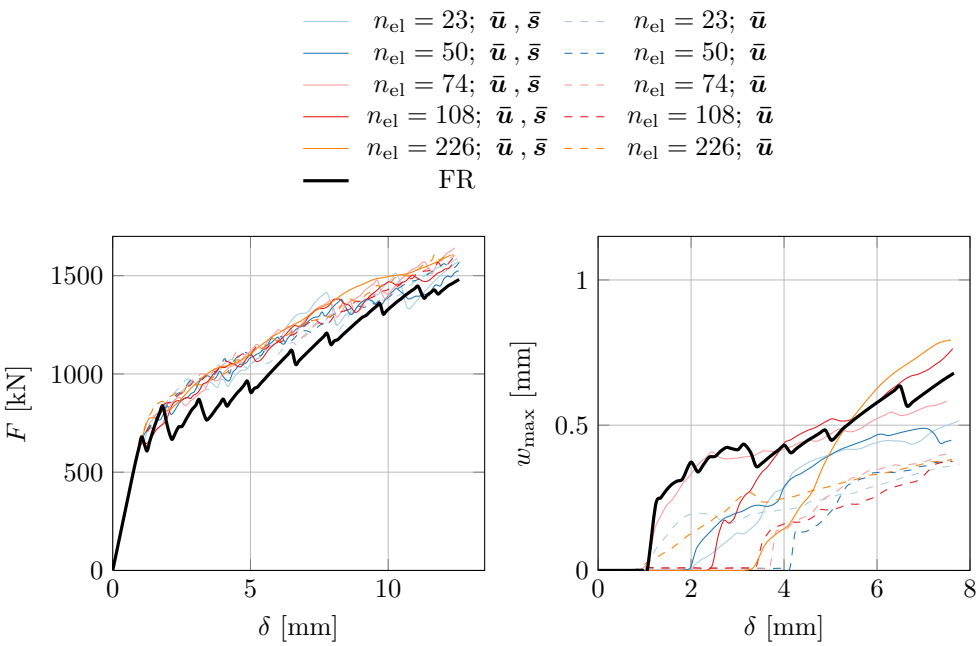

Figure 6.5: External load (left), F, and maximum crack width (right), w_{max}, versus mid-span deflection, δ. The presented results are from a fully-resolved analysis and from enriched $(\bar{\boldsymbol{u}}, \bar{\boldsymbol{s}})$ and unenriched $(\bar{\boldsymbol{u}})$ two-scale analyses using a single-sized RVE and n_{el} finite elements in the large-scale mesh.

Paper C: **On a volume averaged measure of macroscopic reinforcement slip in two-scale modelling of reinforced concrete**
In **Paper C**, the two-scale model from **Paper B** is further developed. Namely, a Neumann-type boundary condition is considered for the macroscopic reinforcement slip. In contrast to **Paper B**, where the effective slip was prescribed only at the boundary of the RVE, Lagrange multipliers are used to impose the macroscopic slip and its gradient in the volume of the RVE. To this end, suitable micro-to-macro transitions for the slip and slip gradient are proposed.

The Neumann-type boundary condition on effective slip field is then combined with the Dirichlet-type boundary condition on the effective displacement field, and thus creating a new alternative to be used in two-scale modelling. For the numerical simulations, the reinforcement pull-through test from **Paper B** is repeated with both old and new type of boundary conditions. Furthermore, the impact of the novel boundary conditions on predicting the crack widths is studied on the example of the deep beam in four-point bending. The main results of **Paper C** can be summarised as follows:

- Effective slip versus transfer stress response of the RVE was no longer size dependent due to a consistent volumetric definition of effective slip and its gradient, see Figure 6.6.
- Globally, the volumetric formulation produced more consistent amplitudes of effective slip fluctuations compared to the boundary formulation from **Paper B**, see Figure 6.7.
- Crack width predictions, although still mostly underestimated, were more consistent and had a lower variance when the macroscopic slip was prescribed in the volume of the RVE, see Figure 6.8.

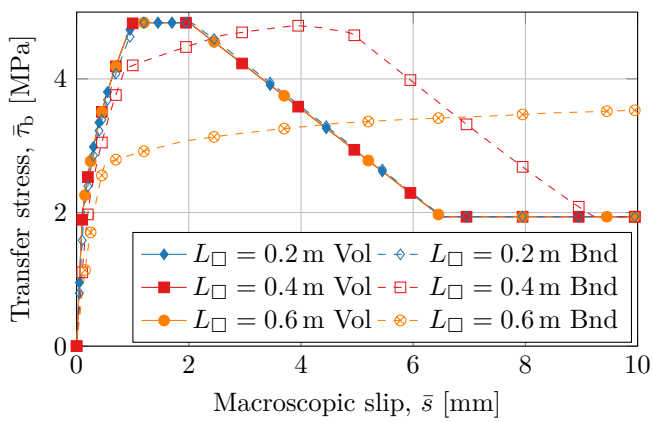

Figure 6.6: Transfer stress versus macroscopic slip relations for RVEs of different sizes, $L_\square$, when prescribing the slip in the volume (Vol, Paper C) and at boundary (Bnd, Paper B) of the RVE.

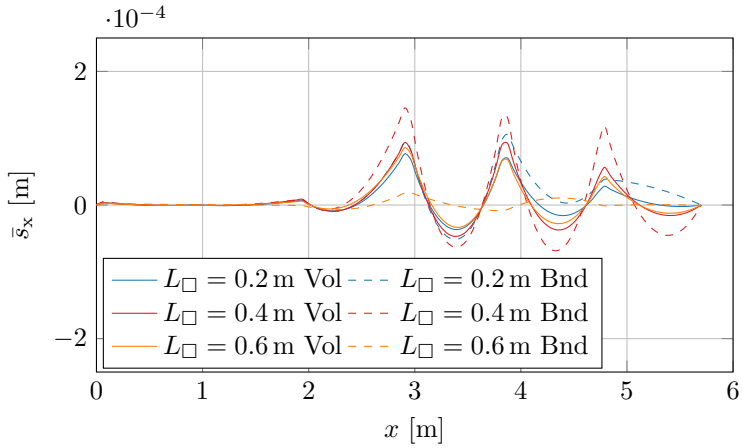

Figure 6.7: Macroscopic reinforcement slip profile for different RVE sizes, $L_\square$, using volumetric (Vol, Paper C) and boundary (Bnd, Paper B) definition of the macroscopic slip.

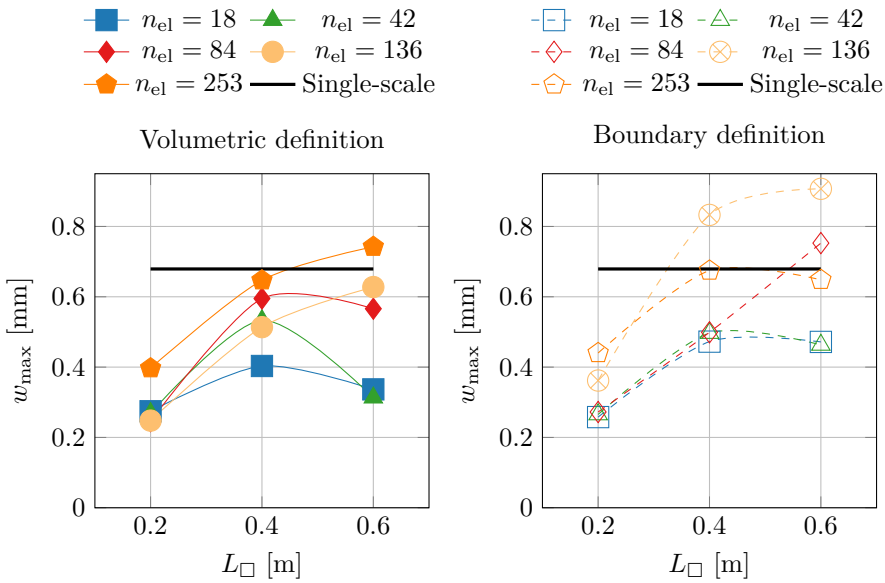

Figure 6.8: Maximum crack width, $w_{\max}$ given by the two-scale model with n_{el} large-scale finite elements for different RVE sizes, $L_\square$. Either volumetric (left, Paper C) or boundary (right, Paper B) definition of the effective reinforcement slip was used.

Paper D: **Two-scale modelling of reinforced concrete deep beams: Choice of unit cell and comparison with single-scale modelling**

In **Paper D**, the two-scale model from **Paper A** is used to analyse a few examples of reinforced concrete deep beams with different reinforcement layouts, for which experimental results were readily available. In contrast to the beams studied **Papers A**–**C**, some of the chosen beams were not uniformly reinforced. As a result, a single RVE can no longer be used to represent the substructure, and the macroscopic domains are further subdivided into regions with approximately uniform reinforcement layout, see Figure 6.9.

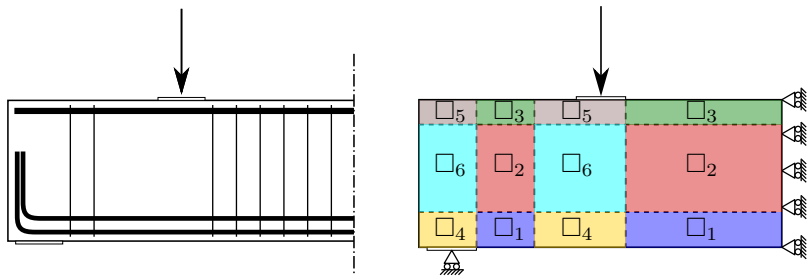

(a) Reinforcement layout (b) Macroscopic subdivision

Figure 6.9: Reinforcement layout (a) and macroscopic subdivision (b) for one of the modelled deep beams. Due to symmetry, only half of the beam is modelled.

An automatic unit cell generation scheme is implemented, whereby an RVE of a given size can be easily created by specifying only few parameters such as the diameter and spacing of rebars in each direction, side length and thickness, see Figure 6.10.

For boundary conditions, the Dirichlet-Dirichlet combination from **Paper A** is employed. The FE^2 method is then used to analyse the beams with different sizes of the subscale unit cells and the results are compared with single-scale analyses and experiments. The main results of **Paper D** can be summarised as follows:

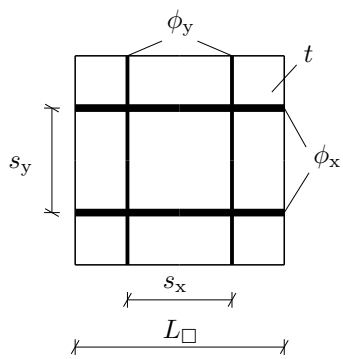

Figure 6.10: A generic RVE with the necessary parameters for multiscale analysis of uniformly reinforced structures in plane stress.

- It is possible to use the developed two-scale model for non-uniformly reinforced structures by suitable division of the macroscopic domain into subdomains with approximately uniform reinforcement layout.
- The size of the unit cell in the subdomains did not significantly influence the global load–deflection results, see Figure 6.11.
- Although both single- and two-scale models underestimated the deflection of the beams, the maximum load was predicted reasonably well.

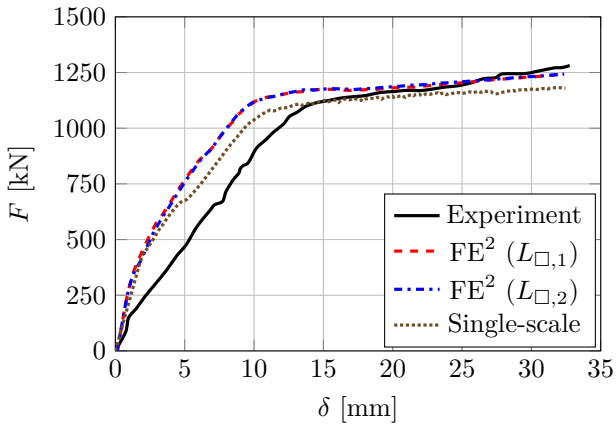

Figure 6.11: External force, F, versus mid-span deflection, δ, response for the reinforced concrete beam from Figure 6.9. In the graphs, results from two FE^2 analyses using different sizes of the RVEs and a single-scale analysis are compared with the experimental results from Aguilar et al. [2].

Paper E: **Upscaling of three-dimensional reinforced concrete representative volume elements to effective beam and plate models**
In **Paper E**, the response of a reinforced concrete RVE is upscaled to effective beam and plate models, as briefly summarised in Sections 5.3 and 5.4. Since strongly periodic boundary conditions are considered for the RVE, an efficient scheme for periodic mesh generation is outlined. The effective in-plane strain tensor $[\bar{\boldsymbol{u}} \otimes \boldsymbol{\nabla}_{\mathrm{p}}]^{\mathrm{sym}}$ and curvature tensor $[\boldsymbol{\nabla}_{\mathrm{p}} \bar{w} \otimes \boldsymbol{\nabla}_{\mathrm{p}}]$ is then imposed on the RVE with special modified tetrahedral finite elements. These elements treat the macroscopic variables as additional degrees of freedom, providing a periodic solution of the RVE problem.

For the numerical examples, the effective beam and plate models are used to study the qualitative response of the concrete structure under uniaxial tension and bending. Furthermore, a series of tests on reinforced concrete panels subjected to bending and membrane loads is simulated, and the the effective response is compared with experimental results. The main results of **Paper E** can be summarised as follows:

- For the Euler-Bernoulli beam model, the effective response of the RVE followed the well-known response of a reinforced concrete cross-section in tension and bending, see Figures 6.12 and 6.13.
- The influecne of the RVE size on the effective response was negligible.
- The response of the RVE model agreed well with the experiments, and the average crack spacings were reflected in a satisfactory way, see Figure 6.14 for an example of the effective response and strain localisation pattern at the surface of the RVE.

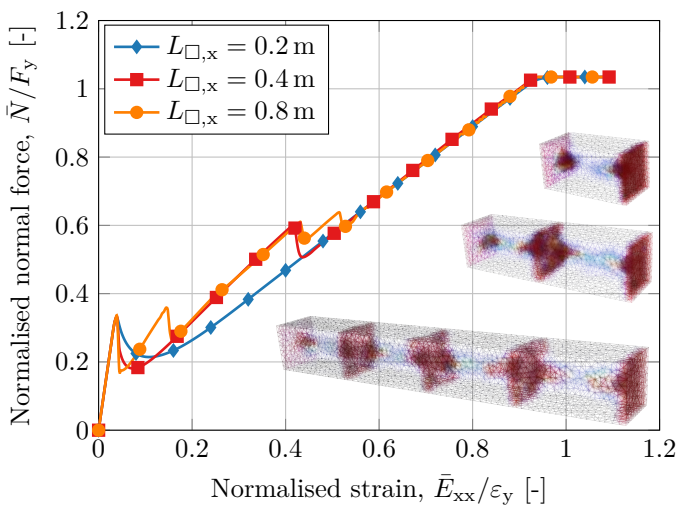

Figure 6.12: Normalised effective normal force versus normalised macroscopic axial strain for three different beam RVEs.

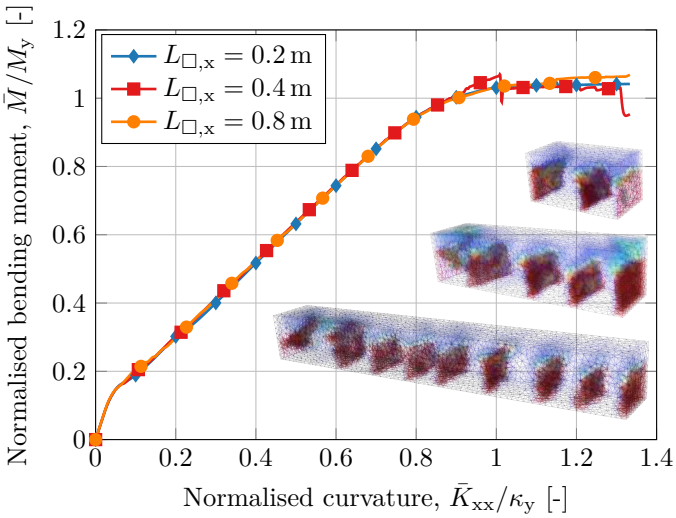

Figure 6.13: Normalised effective bending moment versus normalised macroscopic curvature for three different beam RVEs.

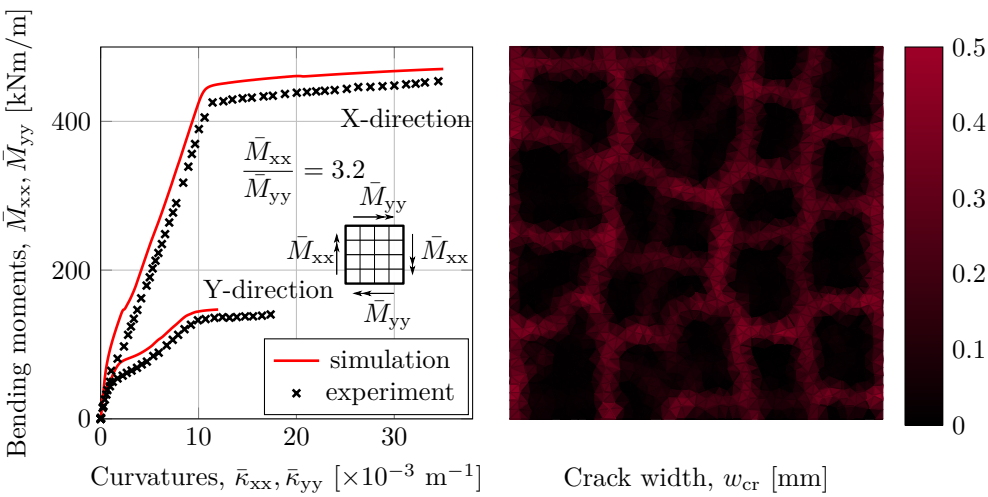

Figure 6.14: Effective bending moment versus macroscopic curvature relations for a reinforced concrete unit cell in biaxial bending (left). Strain localisation pattern at the bottom surface of the RVE (right). Experimental results from Polak and Vecchio [84].

7 Conclusions and future work

7.1 Conclusions

The goal of this work was to extend the multiscale modelling methodology to reinforced concrete structures in order to allow for efficient study of crack formation in large-scale structures. To this end, the Variationally Consistent Homogenisation (VCH) was used as a basis for establishing the two-scale models for reinforced concrete. Representative Volume Elements (RVEs) containing reinforcement grids, in which the reinforcment bars are orthogonal, were considered to be well-suited for multiscale analyses of large-scale reinforced concrete structures. To model the steel reinforcement, beam/truss elements and a Von Mises elastoplastic material model with strain hardening was used. In order to take the steel/concrete bond into account, the interface around the rebars was resolved using interface elements, and a suitable bond-slip response was used as the traction-separation law in the tangential direction.

For the boundary conditions on the RVEs, the classical Dirichlet, Neumann and periodic boundary conditions were used as a starting point. Since the solution of the RVE problem produces displacement fields in concrete and steel, different combination of the classical boundary conditions can be used for the two materials. In this thesis, a few different combinations of the aforementioned boundary conditions were developed and studied. Dirichlet and periodic boundary conditions provided a consistent response of the RVE and were suitable for two-scale models.

Since large-scale reinforced concrete structures are in practice rarely analysed with three-dimensional detailed models, a few commonly used structural models were chosen for upscaling. First, for large structures loaded in-plane, such as walls, an effective solid in plane stress model was developed. Furthermore, structural elements with large span-to-depth ratio such as reinforced concrete beams or columns can be suitably represented with beam models. To this end, the response of the RVE was homogenised to an effective Euler-Bernoulli beam model. Additionally, large scale out-of-plane loaded structures, such as bridge decks, are often modelled with shell/plate elements. Hence, the RVE was also upscaled to an effective Kirchhoff-Love model.

In order to investigate the significance of the slip in the two-scale model, different approaches were considered and evaluated. Initially, the slip was considered to vary only at the subscale. Subsequently, slip transfer across large-scale elements was enabled. To this end, a novel macroscopic reinforcement slip field, representing the displacement of the reinforcement grid relative to the concrete, was proposed and incorporated into the existing model of effective solid in plane stress. In addition to the displacement fields in concrete and steel, the macroscopic slip and its gradient were imposed either at the boundary (Dirichlet boundary condition) or in the volume (Neumann boundary condition) of the RVE.

Regarding the local results, such as crack widths, the predictions given by the multiscale models underestimated the single-scale solution in most cases. However, the estimates improved and became more consistent across multiple analyses upon introducing the macroscopic slip variable and suitable boundary conditions, which prescribe the slip in

the volume of the RVE rather than only at its boundary. The volumetric definition of macroscopic reinforcement slip resulted in an RVE-size independent interpretation of the slip variable, and improved the objectivity of the model with respect to the large-scale mesh and RVE size.

The main conclusion from the present work is that the developed two-scale models simulate the general structural behaviour well, i.e., the multiscale results agreed well with single-scale solution in terms of load–deflection curves, deformation shapes and average strains. Furthermore, not only uniformly reinforced, but also structures with non-uniform reinforcement layout can be analysed with the developed models by appropriate assignment of the unit cells in different regions of the structure. The response of structures subjected to complex membrane and bending loads was also captured well by the developed two-scale models. The FE^2 method, upon proper parallelisation, shows potential in saving computational time and thus making the developed multiscale formulation attractive for implementation in finite element solvers.

7.2 Future work

For future work, multiple areas of interest can be identified. First of all, the multiscale formulation can be extended also to other popular structural models, such as Timoshenko beam and Mindlin plate. This will allow for modelling a wider range of engineering structures for which the Euler-Bernoulli and Kirchhoff-Love kinematics are not enough, e.g., shorter beams or thicker shells/plates. If needed, the new models can be then enriched by the macroscopic slip variable, and the effect of it on both large-scale and subscale response should be studied in more detail.

Another suggestion is to enhance the fidelity of the RVE models and to study the impact of it on large-scale predictions. Examples include different crack modelling techniques as well as different constitutive models for plain concrete, allowing for a more refined study of subscale crack growth in detail. In order to obtain high fidelity models which can be used for modelling structural performance in the serviceability limit state, the structural problem can be coupled with ion ingress/corrosion problem, which have already been studied with multiscale methods. If higher resolution results are needed, the concrete itself could be resolved in more detail by modelling the aggregates and cement.

Since the focus of this work was put on the serviceability limit state (SLS), a natural extension of the presented techniques is to study failure of structures in the ultimate limit state (ULS). Macroscopic localisation, although omitted in this work, can be considered in the models. Two-scale models, which consider upscaling of microscopic fracture patterns to a macroscopic crack, e.g., by means of continuous-discontinuous homogenisation or smeared micro-to-macro transitions, are already available today. Additionally, the model can be extended from quasi-static to dynamic problems. As concrete is a strain-rate dependent material, accurate structural predictions in large-scale structures subjected to dynamic loads are certainly of interest.

In order to use the developed techniques in practice, further verification and improvements of the numerical performance are necessary. To this end, the multiscale models should be applied to real-world case studies. Subsequently, the focus should be put on benchmarking against industry best-practices in modelling of large-scale reinforced concrete structures. Algorithmic improvements in terms of parallelisation, speed-up procedures, adaptivity, numerical model reduction or machine learning could be utilised to make the methods more attractive.

Finally it is noted that the models studied in this work could are also suitable to study other types of composites. Among those, special consideration can be given to textile reinforced concrete structures, due to their uniform reinforcement layouts.

References

[1] ACI Committee 408. *ACI 408.2R Report on bond of steel reinforcing bars under cyclic loads*. Tech. rep. American Concrete Institute, 2012.

[2] G. Aguilar, A. B. Matamoros, G. J. Parra-Montesinos, J. A. Ramirez, and J. K. Wight. Experimental Evaluation of Design Procedures for Shear Strength of Deep Reinforced Concrete Beams. *ACI Structural Journal* **99**.4 (2002), 539–548. DOI: 10.14359/12123.

[3] Z. Bažant. Mechanics of Distributed Cracking. *Applied Mechanics Reviews* **39**.5 (1986), 675–705. DOI: 10.1115/1.3143724.

[4] Z. Bažant and B. Oh. Crack band theory of concrete. *Materials and Structures* **16** (1983), 155–177. DOI: 10.1007/BF02486267.

[5] T. Belytschko and T. Black. Elastic crack growth in finite elements with minimal remeshing. *International Journal for Numerical Methods in Engineering* **45**.5 (1999), 601–620. DOI: 10.1002/(SICI)1097-0207(19990620)45:5<601::AID-NME598>3.0.CO;2-S.

[6] T. Belytschko and J.-H. Song. Coarse-graining of multiscale crack propagation. *International Journal for Numerical Methods in Engineering* **81**.5 (2010), 537–563. DOI: 10.1002/nme.2694.

[7] M. R. Ben Romdhane and F.-J. Ulm. Computational mechanics of the steel-concrete interface. *International Journal for Numerical and Analytical Methods in Geomechanics* **26**.2 (2002), 99–120. DOI: 10.1002/nag.158.

[8] N. Benkemoun, M. Hautefeuille, J.-B. Colliat, and A. Ibrahimbegovic. Failure of heterogeneous materials: 3D meso-scale FE models with embedded discontinuities. *International Journal for Numerical Methods in Engineering* **82**.13 (2010), 1671–1688. DOI: 10.1002/nme.2816.

[9] H. Broo, M. Plos, K. Lundgren, and B. Engström. Simulation of shear-type cracking and failure with non-linear finite-element method. *Magazine of Concrete Research* **59**.9 (2007), 673–687. DOI: 10.1680/macr.2007.59.9.673.

[10] V. I. Carbone and M. Codegone. Behaviour of a reinforced concrete by homogenization technique. *Mechanics Research Communications* **27**.1 (2000), 95–100. DOI: 10.1016/S0093-6413(00)00067-7.

[11] CEN. Eurocode 2: Design of concrete structures. Part 1: General rules and rules for buildings. *European Committee for Standardization* (2004).

[12] E. W. C. Coenen, V. G. Kouznetsova, and M. G. D. Geers. Computational homogenization for heterogeneous thin sheets. *International Journal for Numerical Methods in Engineering* **83**.8–9 (2010), 1180–1205. DOI: 10.1002/nme.2833.

[13] E. W. C. Coenen, V. G. Kouznetsova, and M. G. D. Geers. Multi-scale continuous-discontinuous framework for computational-homogenization-localization. *Journal of the Mechanics and Physics of Solids* **60**.8 (2012), 1486–1507. DOI: 10.1016/j.jmps.2012.04.002.

[14] E. W. C. Coenen, V. G. Kouznetsova, E. Bosco, and M. G. D. Geers. A multi-scale approach to bridge microscale damage and macroscale failure: A nested

computational homogenization-localization framework. *International Journal of Fracture* **178**.1–2 (2012), 157–178. DOI: 10.1007/s10704-012-9765-4.

[15] L. Contrafatto, M. Cuomo, and F. Fazio. An enriched finite element for crack opening and rebar slip in reinforced concrete members. *International Journal of Fracture* **178**.1 (2012), 33–50. DOI: 10.1007/s10704-012-9723-1.

[16] J. S. Damtoft, J. Lukasik, D. Herfort, D. Sorrentino, and E. M. Gartner. Sustainable development and climate change initiatives. *Cement and Concrete Research* **38**.2 (2008), 115–127. DOI: 10.1016/j.cemconres.2007.09.008.

[17] A. Daoud, O. Maurel, and C. Laborderie. 2D mesoscopic modelling of bar-concrete bond. *Engineering Structures* **49** (2013), 696–706. DOI: 10.1016/j.engstruct.2012.11.018.

[18] R. de Borst. Fracture in quasi-brittle materials: a review of continuum damage-based approaches. *Engineering Fracture Mechanics* **69**.2 (2002), 95–112. DOI: 10.1016/S0013-7944(01)00082-0.

[19] R. de Borst, J. J. C. Remmers, A. Needleman, and M.-A. Abellan. Discrete vs smeared crack models for concrete fracture: bridging the gap. *International Journal for Numerical and Analytical Methods in Geomechanics* **28**.7-8 (2004), 583–607. DOI: 10.1002/nag.374.

[20] M. J. DeJong, M. A. N. Hendriks, and J. G. Rots. Sequentially linear analysis of fracture under non-proportional loading. *Engineering Fracture Mechanics* **75**.18 (2008), 5042–5056. DOI: 10.1016/j.engfracmech.2008.07.003.

[21] N. Dominguez, D. Brancherie, L. Davenne, and A. Ibrahimbegovic. Prediction of crack pattern distribution in reinforced concrete by coupling a strong discontinuity model of concrete cracking and a bond-slip of reinforcement model. *Engineering Computations* **22**.5/6 (2005), 558–582. DOI: 10.1108/02644400510603014.

[22] N. Dominguez, M. A. Fernández, and A. Ibrahimbegovic. Enhanced solid element for modelling of reinforced concrete structures with bond-slip. *Computers and Concrete* **7**.4 (2010), 347–364. DOI: 10.12989/cac.2010.7.4.347.

[23] F. Feyel. A multilevel finite element method (FE2) to describe the response of highly non-linear structures using generalized continua. *Computer Methods in Applied Mechanics and Engineering* **192**.28 (2003), 3233–3244. DOI: 10.1016/S0045-7825(03)00348-7.

[24] F. Feyel and J.-L. Chaboche. FE2 multiscale approach for modelling the elastovisco-plastic behaviour of long fibre SiC/Ti composite materials. *Computer Methods in Applied Mechanics and Engineering* **183**.3 (2000), 309–330. DOI: 10.1016/S0045-7825(99)00224-8.

[25] Fib. *Bond of reinforcement in concrete: state-of-the-art report*. Bulletin 10 (fib Fédération internationale du béton). International Federation for Structural Concrete, 2000.

[26] Fib. *Model code for concrete structures 2010*. Wiley-VCH Verlag GmbH & Co. KGaA, 2013. DOI: 10.1002/9783433604090.

[27] D. Floros and O. A. Ingason. "Modelling and simulation of reinforced concrete beams - Coupled analysis of imperfectly bonded reinforcement in fracturing concrete". Master's thesis. 2013.

[28] T. Fries and T. Belytschko. The extended/generalized finite element method: An overview of the method and its applications. *International Journal for Numerical Methods in Engineering* **84**.3 (2010), 253–304. DOI: 10.1002/nme.2914.

[29] M. Geers, V. G. Kouznetsova, and W. A. M. Brekelmans. MultiScale First-Order and Second-Order Computational Homogenization of Microstructures towards Continua. *International Journal for Multiscale Computational Engineering* **1**.4 (2003), 371–386. DOI: 10.1615/IntJMultCompEng.v1.i4.40.

[30] P. Grassl and M. Jirásek. Meso-scale approach to modelling the fracture process zone of concrete subjected to uniaxial tension. *International Journal of Solids and Structures* **47**.7 (2010), 957–968. DOI: 10.1016/j.ijsolstr.2009.12.010.

[31] P. Grassl and M. Jirásek. Plastic model with non-local damage applied to concrete. *International Journal for Numerical and Analytical Methods in Geomechanics* **30**.1 (2006), 71–90. DOI: 10.1002/nag.479.

[32] M. Hallgren and M. Bjerke. Non-linear finite element analyses of punching shear failure of column footings. *Cement and Concrete Composites* **24**.6 (2002), 491–496. DOI: 10.1016/S0958-9465(01)00065-8.

[33] M. Hallgren, I. Eriksson, and N. Karlsson. "Numerical Simulations of a Concrete Bridge Deck Loaded to Shear Failure". *High Tech Concrete: Where Technology and Engineering Meet*. Ed. by D. A. Hordijk and M. Luković. Springer International Publishing, 2018, pp. 1898–1906. DOI: 10.1007/978-3-319-59471-2.

[34] M. A. Hendriks and J. G. Rots. Sequentially linear versus nonlinear analysis of RC structures. *Engineering Computations* **30**.6 (2013), 792–801. DOI: 10.1108/EC-May-2012-0105.

[35] T. Herwig and W. Wagner. On a robust FE2 model for delamination analysis in composite structures. *Composite Structures* **201** (2018), 597–607. DOI: 10.1016/j.compstruct.2018.06.033.

[36] R. Hill. Elastic properties of reinforced solids: Some theoretical principles. *Journal of the Mechanics and Physics of Solids* **11**.5 (1963), 357–372. DOI: 10.1016/0022-5096(63)90036-X.

[37] A. Hillerborg, M. Modéer, and P.-E. Petersson. Analysis of crack formation and crack growth in concrete by means of fracture mechanics and finite elements. *Cement and Concrete Research* **6**.6 (1976), 773–781. DOI: 10.1016/0008-8846(76)90007-7.

[38] T. J. R. Hughes, G. R. Feijóo, L. Mazzei, and J.-B. Quincy. The variational multiscale method - a paradigm for computational mechanics. *Computer Methods in Applied Mechanics and Engineering* **166**.1 (1998), 3–24. DOI: 10.1016/S0045-7825(98)00079-6.

[39] M. Huguet, S. Erlicher, P. Kotronis, and F. Voldoire. Stress resultant nonlinear constitutive model for cracked reinforced concrete panels. *Engineering Fracture Mechanics* **176** (May 2017), 375–405. DOI: 10.1016/j.engfracmech.2017.02.027.

[40] A. Ibrahimbegovic, A. Boulkertous, L. Davenne, and D. Brancherie. Modelling of reinforced-concrete structures providing crack-spacing based on X-FEM, ED-FEM and novel operator split solution procedure. *International Journal for Numerical Methods in Engineering* **83**.4 (2010), 452–481. DOI: 10.1002/nme.2838.

[41] A. Ibrahimbegovic and S. Melnyk. Embedded discontinuity finite element method for modeling of localized failure in heterogeneous materials with structured mesh: an alternative to extended finite element method. *Computational Mechanics* **40**.1 (2007), 149–155. DOI: 10.1007/s00466-006-0091-4.

[42] S. Invernizzi, D. Trovato, M. A. N. Hendriks, and A. V. van de Graaf. Sequentially linear modelling of local snap-back in extremely brittle structures. *Engineering Structures* **33**.5 (2011), 1617–1625. DOI: 10.1016/j.engstruct.2011.01.031.

[43] P. Irawan and K. Maekawa. Path-dependent nonlinear analysis of reinforced concrete shells. *Doboku Gakkai Ronbunshu* 557 (1997), 121–134. DOI: 10.2208/jscej.1997.557_121.

[44] M. Jirásek. *Modeling of Localized Inelastic Deformation*. Prague, 2016.

[45] M. Jirásek. Nonlocal models for damage and fracture: Comparison of approaches. *International Journal of Solids and Structures* **35**.31 (1998), 4133–4145. DOI: 10.1016/S0020-7683(97)00306-5.

[46] M. Jirásek and P. Grassl. Evaluation of directional mesh bias in concrete fracture simulations using continuum damage models. *Engineering Fracture Mechanics* **75**.8 (2008), 1921–1943. DOI: 10.1016/j.engfracmech.2007.11.010.

[47] E. Karavelić, M. Nikolić, A. Ibrahimbegovic, and A. Kurtović. Concrete meso-scale model with full set of 3D failure modes with random distribution of aggregate and cement phase. Part I: Formulation and numerical implementation. *Computer Methods in Applied Mechanics and Engineering* **344** (2019), 1051–1072. DOI: 10.1016/j.cma.2017.09.013.

[48] A. T. Karttunen, J. N. Reddy, and J. Romanoff. Two-scale micropolar plate model for web-core sandwich panels. *International Journal of Solids and Structures* **170** (2019), 82–94. DOI: 10.1016/j.ijsolstr.2019.04.026.

[49] V. Kouznetsova, W. A. M. Brekelmans, and F. P. T. Baaijens. An approach to micro-macro modeling of heterogeneous materials. *Computational Mechanics* **27**.1 (2001), 37–48. DOI: 10.1007/s004660000212.

[50] R. Lackner and H. A. Mang. Scale Transition in Steel-Concrete Interaction. I: Model. *Journal of Engineering Mechanics* **129**.4 (2003), 393–402. DOI: 10.1061/(ASCE)0733-9399(2003)129:4(393).

[51] R. Lackner and H. A. Mang. Scale Transition in Steel-Concrete Interaction. II: Applications. *Journal of Engineering Mechanics* **129**.4 (2003), 403–413. DOI: 10.1061/(ASCE)0733-9399(2003)129:4(403).

[52] F. Larsson, K. Runesson, and F. Su. Variationally consistent computational homogenization of transient heat flow. *International Journal for Numerical Methods in Engineering* **81**.13 (2010), 1659–1686. DOI: 10.1002/nme.2747.

[53] J.-L. Le, M. DesHarnais, B. Xue, S. D. Pang, and H. Du. A two-scale computational model for thermomechanical analysis of reinforced concrete frames. *Engineering Structures* **105** (2015), 137–151. DOI: 10.1016/j.engstruct.2015.09.041.

[54] H. R. Lotfi and P. B. Shing. Embedded representation of fracture in concrete with mixed finite elements. *International Journal for Numerical Methods in Engineering* **38**.8 (1995), 1307–1325. DOI: 10.1002/nme.1620380805.

[55] K. Lundgren. Bond between ribbed bars and concrete. Part 1: Modified model. *Magazine of Concrete Research* **57**.7 (2005), 371–382. DOI: 10.1680/macr.2005.57.7.371.

[56] K. Lundgren and K. Gylltoft. A model for the bond between concrete and reinforcement. *Magazine of Concrete Research* **52**.1 (2000), 53–63. DOI: 10.1680/macr.2000.52.1.53.

[57] K. Lundgren, P. Kettil, K. Z. Hanjari, H. Schlune, and A. S. S. Roman. Analytical model for the bond-slip behaviour of corroded ribbed reinforcement. *Structure and Infrastructure Engineering* **8**.2 (2012), 157–169. DOI: 10.1080/15732470903446993.

[58] D. Markovic and A. Ibrahimbegovic. On micro-macro interface conditions for micro scale based FEM for inelastic behavior of heterogeneous materials. *Computer Methods in Applied Mechanics and Engineering* **193**.48 (2004), 5503–5523. DOI: 10.1016/j.cma.2003.12.072.

[59] P. Mata, A. H. Barbat, and S. Oller. Two-scale approach for the nonlinear dynamic analysis of RC structures with local non-prismatic parts. *Engineering Structures* **30**.12 (2008), 3667–3680. DOI: 10.1016/j.engstruct.2008.06.011.

[60] K. Matouš, M. G. Geers, V. G. Kouznetsova, and A. Gillman. A review of predictive nonlinear theories for multiscale modeling of heterogeneous materials. *Journal of Computational Physics* **330** (2017), 192–220. DOI: 10.1016/j.jcp.2016.10.070.

[61] J. Mazars and G. Pijaudier-Cabot. Continuum damage theory-application to concrete. *Journal of Engineering Mechanics* **115**.2 (1989), 345–365. DOI: 10.1061/(ASCE)0733-9399(1989)115:2(345).

[62] J. Mazars. A description of micro- and macroscale damage of concrete structures. *Engineering Fracture Mechanics* **25**.5 (1986), 729–737. DOI: 10.1016/0013-7944(86)90036-6.

[63] B. C. N. Mercatoris and T. J. Massart. A coupled two-scale computational scheme for the failure of periodic quasi-brittle thin planar shells and its application to masonry. *International Journal for Numerical Methods in Engineering* **85**.9 (2011), 1177–1206. DOI: 10.1002/nme.3018.

[64] C. Miehe and C. G. Bayreuther. On multiscale FE analyses of heterogeneous structures: from homogenization to multigrid solvers. *International Journal for Numerical Methods in Engineering* **71**.10 (2007), 1135–1180. DOI: 10.1002/nme.1972.

[65] J. Mosler and G. Meschke. 3D modelling of strong discontinuities in elastoplastic solids: Fixed and rotating localization formulations. *International Journal for Numerical Methods in Engineering* **57**.11 (2003), 1553–1576. DOI: 10.1002/nme.731.

[66] A. Moyeda and J. Fish. Multiscale analysis of solid, waffle, ribbed and hollowcore reinforced concrete slabs. *Computer Methods in Applied Mechanics and Engineering* **348** (2019), 139–156. DOI: 10.1016/j.cma.2019.01.022.

[67] R. Muhamad, M. S. Mohamed Ali, D. Oehlers, and A. Hamid Sheikh. Load-slip relationship of tension reinforcement in reinforced concrete members. *Engineering Structures* **33**.4 (2011), 1098–1106. DOI: 10.1016/j.engstruct.2010.12.022.

[68] C. Nader, P. Rossi, and J.-L. Tailhan. Numerical strategy for developing a probabilistic model for elements of reinforced concrete. *Structural Concrete* **18**.6 (2017), 883–892. DOI: 10.1002/suco.201600217.

[69] V. P. Nguyen, O. Lloberas-Valls, M. Stroeven, and L. J. Sluys. Homogenization-based multiscale crack modelling: From micro-diffusive damage to macro-cracks. *Computer Methods in Applied Mechanics and Engineering* **200**.9-12 (2011), 1220–1236. DOI: 10.1016/j.cma.2010.10.013.

[70] V. P. Nguyen, M. Stroeven, and L. J. Sluys. Multiscale failure modeling of concrete: Micromechanical modeling, discontinuous homogenization and parallel computations. *Computer Methods in Applied Mechanics and Engineering* **201-204** (2012), 139–156. DOI: 10.1016/j.cma.2011.09.014.

[71] M. Nikolić, X. N. Do, A. Ibrahimbegovic, and Ž. Nikolić. Crack propagation in dynamics by embedded strong discontinuity approach: Enhanced solid versus discrete lattice model. *Computer Methods in Applied Mechanics and Engineering* **340** (2018), 480–499. DOI: 10.1016/j.cma.2018.06.012.

[72] F. Nilenius, F. Larsson, K. Lundgren, and K. Runesson. Computational homogenization of diffusion in three-phase mesoscale concrete. *Computational Mechanics* **54**.2 (2014), 461–472. DOI: 10.1007/s00466-014-0998-0.

[73] F. Nilenius, F. Larsson, K. Lundgren, and K. Runesson. FE2 Method for Coupled Transient Diffusion Phenomena in Concrete. *Journal of Engineering Mechanics* **141**.2 (2015), 4014110. DOI: 10.1061/(ASCE)EM.1943-7889.0000684.

[74] F. Nilenius, F. Larsson, K. Lundgren, and K. Runesson. Macroscopic diffusivity in concrete determined by computational homogenization. *International Journal for Numerical and Analytical Methods in Geomechanics* **37**.11 (2013), 1535–1551. DOI: 10.1002/nag.2097.

[75] F. Nilenius, F. Larsson, K. Lundgren, and K. Runesson. Mesoscale modelling of crack-induced diffusivity in concrete. *Computational Mechanics* **55**.2 (2015), 359–370. DOI: 10.1007/s00466-014-1105-2.

[76] J. Oliver, M. Caicedo, E. Roubin, J. Hernández, and A. Huespe. Multi-scale (FE2) analysis of material failure in cement/aggregate-type composite structures. *Computational Modelling of Concrete Structures* (2014), 39–49.

[77] J. Oliver, M. Cervera, S. Oller, and J. Lubliner. "Isotropic damage models and smeared crack analysis of concrete". *Computer Aided Analysis and Design of Concrete Structures*. 1990, pp. 945–957.

[78] N. S. Ottosen and M. Ristinmaa. Thermodynamically based fictitious crack/interface model for general normal and shear loading. *International Journal of Solids and Structures* **50**.22-23 (2013), 3555–3561. DOI: 10.1016/j.ijsolstr.2013.06.019.

[79] B. Patzák. OOFEM - an object-oriented simulation tool for advanced modeling of materials and structures. *Acta Polytechnica* **52**.6 (2012), 59–66.

[80] R. H. J. Peerlings, R. De Borst, W. A. M. Brekelmans, and J. H. P. De Vree. Gradient enhanced damage for quasi-brittle materials. *International Journal for Numerical Methods in Engineering* **39**.19 (1996), 3391–3403. DOI: 10.1002/(SICI)1097-0207(19961015)39:19<3391::AID-NME7>3.0.CO;2-D.

[81] M. Petracca, L. Pelà, R. Rossi, S. Oller, G. Camata, and E. Spacone. Multiscale computational first order homogenization of thick shells for the analysis of out-

of-plane loaded masonry walls. *Computer Methods in Applied Mechanics and Engineering* **315** (2017), 273–301. DOI: 10.1016/j.cma.2016.10.046.

[82] B. H. Pham, D. Brancherie, L. Davenne, and A. Ibrahimbegovic. Stress-resultant models for ultimate load design of reinforced concrete frames and multi-scale parameter estimates. *Computational Mechanics* **51**.3 (2013), 347–360. DOI: 10.1007/s00466-012-0734-6.

[83] M. A. Polak and F. J. Vecchio. Nonlinear Analysis of Reinforced-Concrete Shells. *Journal of Structural Engineering* **119**.12 (1993), 3439–3462. DOI: 10.1061/(ASCE)0733-9445(1993)119:12(3439).

[84] M. A. Polak and F. J. Vecchio. Reinforced Concrete Shell Elements Subjected to Bending and Membrane Loads. *ACI Structural Journal* **91**.3 (1994), 261–268. DOI: 10.14359/4353.

[85] M. Praster, M. Klassen, and S. Klinkel. An adaptive FE2 approach for fiber-matrix composites. *Computational Mechanics* (2018). DOI: 10.1007/s00466-018-1652-z.

[86] B. Reinaldo Goncalves, J. Jelovica, and J. Romanoff. A homogenization method for geometric nonlinear analysis of sandwich structures with initial imperfections. *International Journal of Solids and Structures* **87** (2016), 194–205. DOI: 10.1016/j.ijsolstr.2016.02.009.

[87] E. A. Rodrigues, O. L. Manzoli, L. A. G. Bitencourt, T. N. Bittencourt, and M. Sánchez. An adaptive concurrent multiscale model for concrete based on coupling finite elements. *Computer Methods in Applied Mechanics and Engineering* **328** (2018), 26–46. DOI: 10.1016/j.cma.2017.08.048.

[88] J. G. Rots, P. Nauta, G. M. A. Kusters, and J. Blaauwendraad. Smeared Crack Approach and Fracture Localization in Concrete. *Heron* **30**.1 (1985).

[89] J. G. Rots and J. Blaauwendraad. Crack models for concrete: discrete or smeared? Fixed multi-directional or rotating? *Heron* **34**.1 (1989), 3–59.

[90] I. Rukavina, A. Ibrahimbegovic, X. N. Do, and D. Markovic. ED-FEM multi-scale computation procedure for localized failure. *Coupled System Mechanics* **8**.2 (2019), 1–19. DOI: 10.12989/csm.2019.8.2.111.

[91] A. T. Slobbe, M. A. N. Hendriks, and J. G. Rots. Systematic assessment of directional mesh bias with periodic boundary conditions: Applied to the crack band model. *Engineering Fracture Mechanics* **109** (2013), 186–208. DOI: 10.1016/j.engfracmech.2013.06.005.

[92] T. Stankowski, K. Runesson, and S. Sture. Fracture and Slip of Interfaces in Cementitious Composites. I: Characteristics. *Journal of Engineering Mechanics* **119**.2 (1993), 292–314. DOI: 10.1061/(ASCE)0733-9399(1993)119:2(292).

[93] T. Stankowski, K. Runesson, and S. Sture. Fracture and Slip of Interfaces in Cementitious Composites. II: Implementation. *Journal of Engineering Mechanics* **119**.2 (1993), 315–327. DOI: 10.1061/(ASCE)0733-9399(1993)119:2(315).

[94] B. Sun and Z. Li. Adaptive concurrent multi-scale FEM for trans-scale damage evolution in heterogeneous concrete. *Computational Materials Science* **99** (2015), 262–273. DOI: 10.1016/j.commatsci.2014.12.033.

[95] B. Sun and Z. Li. Adaptive concurrent three-level multiscale simulation for trans-scale process from material mesodamage to structural failure of concrete structures.

International Journal of Damage Mechanics **25**.5 (2016), 750–769. DOI: 10.1177/1056789516648371.

[96] B. Sun and Z. Li. Multi-scale modeling and trans-level simulation from material meso-damage to structural failure of reinforced concrete frame structures under seismic loading. *Journal of Computational Science* **12** (2016), 38–50. DOI: 10.1016/j.jocs.2015.11.003.

[97] E. Svenning, M. Fagerström, and F. Larsson. Computational homogenization of microfractured continua using weakly periodic boundary conditions. *Computer Methods in Applied Mechanics and Engineering* **299** (2016), 1–21. DOI: 10.1016/j.cma.2015.10.014.

[98] E. Svenning, M. Fagerström, and F. Larsson. Localization aligned weakly periodic boundary conditions. *International Journal for Numerical Methods in Engineering* **111**.5 (2017), 493–500. DOI: 10.1002/nme.5483.

[99] E. Svenning, F. Larsson, and M. Fagerström. A two-scale modeling framework for strain localization in solids: XFEM procedures and computational aspects. *Computers and Structures* **211** (2019), 43–54. DOI: 10.1016/j.compstruc.2018.08.003.

[100] E. Svenning, F. Larsson, and M. Fagerström. Two-scale modeling of fracturing solids using a smeared macro-to-micro discontinuity transition. *Computational Mechanics* **60**.4 (2017), 627–641. DOI: 10.1007/s00466-017-1426-z.

[101] R. Tan, M. A. N. Hendriks, M. Geiker, and T. Kanstad. Analytical Calculation Model for Predicting Cracking Behavior of Reinforced Concrete Ties. *Journal of Structural Engineering* **146**.2 (2020), 4019206. DOI: 10.1061/(ASCE)ST.1943-541X.0002510.

[102] I. Temizer and P. Wriggers. A multiscale contact homogenization technique for the modeling of third bodies in the contact interface. *Computer Methods in Applied Mechanics and Engineering* **198**.3 (2008), 377–396. DOI: 10.1016/j.cma.2008.08.008.

[103] J. P. Ulfkjær, K. Steen, and B. Rune. Analytical Model for Fictitious Crack Propagation in Concrete Beams. *Journal of Engineering Mechanics* **121**.1 (1995), 7–15. DOI: 10.1061/(ASCE)0733-9399(1995)121:1(7).

[104] J. F. Unger. An FE2-X1 approach for multiscale localization phenomena. *Journal of the Mechanics and Physics of Solids* **61**.4 (2013), 928–948. DOI: 10.1016/j.jmps.2012.12.010.

[105] J. F. Unger and S. Eckardt. Multiscale modeling of concrete. *Archives of Computational Methods in Engineering* **18**.3 (2011), 341–393. DOI: 10.1007/s11831-011-9063-8.

[106] J. van Mier. *Concrete Fracture: A Multiscale Approach*. CRC Press, 2013. DOI: 10.1201/b12968.

[107] P. Wriggers and S. O. Moftah. Mesoscale models for concrete: Homogenisation and damage behaviour. *Finite Elements in Analysis and Design* **42**.7 (2006), 623–636. DOI: 10.1016/j.finel.2005.11.008.